

Journal Pre-proof

An insight into the mixed quantum mechanical-molecular dynamic simulation of a Zn^{II}-Curcumin complex with a chosen DNA sequence that supports experimental DNA binding investigations



Tanmoy Saha, Subrahmanyam Sappati, Saurabh Das

PII: S0141-8130(23)02199-2

DOI: <https://doi.org/10.1016/j.ijbiomac.2023.125305>

Reference: BIOMAC 125305

To appear in: *International Journal of Biological Macromolecules*

Received date: 28 February 2023

Revised date: 24 May 2023

Accepted date: 30 May 2023

Please cite this article as: T. Saha, S. Sappati and S. Das, An insight into the mixed quantum mechanical-molecular dynamic simulation of a Zn^{II}-Curcumin complex with a chosen DNA sequence that supports experimental DNA binding investigations, *International Journal of Biological Macromolecules* (2023), <https://doi.org/10.1016/j.ijbiomac.2023.125305>

This is a PDF file of an article that has undergone enhancements after acceptance, such as the addition of a cover page and metadata, and formatting for readability, but it is not yet the definitive version of record. This version will undergo additional copyediting, typesetting and review before it is published in its final form, but we are providing this version to give early visibility of the article. Please note that, during the production process, errors may be discovered which could affect the content, and all legal disclaimers that apply to the journal pertain.

An insight into the mixed quantum mechanical-molecular dynamic simulation of a Zn^{II}-Curcumin complex with a chosen DNA sequence that supports experimental DNA binding investigations

¹Tanmoy Saha, ^{2,3}Subrahmanyam Sapani, ¹Saurabh Das*

**¹Department of Chemistry (Inorganic Section), Jadavpur University,
Kolkata – 700 032, INDIA.**

**²Department of Physical Chemistry, Gdańsk University of Technology,
Gdańsk – 80-233, Poland.**

**³Department of Pharmaceutical Technology and Biochemistry,
Gdańsk University of Technology, Gdańsk – 80-233, Poland.**

Short running title: Molecular dynamic simulation of Zn^{II}-Cur with DNA

***Corresponding author: saurabh.das@jadavpuruniversity.in**



Abstract

An important aspect of research pertaining to Curcumin (HCur) is the need to arrest its degradation in aqueous solution and in biological milieu. This may be achieved through complex formation with metal ions. For this reason, a complex of HCur was prepared with Zn^{II} , that is not likely to be active in redox pathways, minimizing further complications. The complex is monomeric, tetrahedral, with one HCur, an acetate and a molecule of water bound to Zn^{II} . It arrests degradation of HCur to a considerable extent that was realized by taking it in phosphate buffer and in biological milieu. The structure was obtained by DFT calculations. Stable adduct formation was identified between optimized structures of HCur and $[Zn(Cur)]$ with DNA (PDB ID: 1BNA) through experiments validated with multiscale modeling approach. Molecular docking studies provide 2D and 3D representations of binding of HCur and $[Zn(Cur)]$ through different non-covalent interactions with the nucleotides of the chosen DNA. Through molecular dynamics simulation, a detailed understanding of binding pattern and key structural characteristics of the generated DNA-complex was obtained following analysis by RMSD, RMSF, radius of gyration, SASA and aspects like formation of hydrogen bonds. Experimental studies provide binding constants for $[Zn(Cur)]$ with calf thymus DNA at 25°C that effectively helps one to realize its high affinity towards DNA. In the absence of an experimental binding study of HCur with DNA, owing to its tendency to degrade in solution, a theoretical analysis of the binding of HCur to DNA is extremely helpful. Besides, both experimental and simulated binding of $[Zn(Cur)]$ to DNA may be considered as a case of pseudo-binding of HCur to DNA. In a way, such studies on interaction with DNA helps one to identify HCur's affinity for cellular target DNA, not realized through experiments. The entire investigation is an understanding of experimental and theoretical approaches that has been compared continuously, being particularly useful when a molecule's interaction with a biological target cannot realized experimentally.

Key Words: Curcumin, Zn^{II} , DFT, molecular docking, molecular dynamic simulation, RMSD, RMSF, radius of gyration, SASA, hydrogen bonds.

Abbreviations: HCur: Curcumin; $[Zn(Cur)]$: Zn^{II} complex of Curcumin;



Introduction:

Curcumin (HCur) is a lipophilic poly-phenol having a lot of potential that has promoted investigations in recent years.¹⁻¹⁰ Given its pharmacological effectiveness, there are a number of issues that prevent it from assuming the position it rightly deserves.¹⁻¹⁰ Research has demonstrated several medicinal benefits of HCur that are useful in treating various medical conditions and pharmacological qualities.^{1,2,4-9,11,12} Clinical trials and *in vivo* investigations demonstrate safety, low toxicity even at dose as high as 12g/day for a period of three months.⁷ However, the molecule fails to achieve its full potential in spite of outstanding pharmacological reports owing to poor solubility in aqueous media. It is prone to degradation in physiological buffer under reducing conditions.¹³⁻¹⁸ The situation gets further complicated because it breaks down into smaller molecules in solution under patho- or physiological conditions making it difficult to assign observed pharmacological action to curcumin itself. Evidence suggests curcumin does not remain in solution as a single unit.^{12,18-20} Consequently, it becomes difficult to say if the findings of pharmacological studies on curcumin are a result of curcumin itself or an outcome of the combined effects of fragments produced in solution following hydrolysis. There is of course the likelihood of curcumin being present in solution as one unit in some proportion, depending upon the extent of hydrolysis in the medium. Like that of others, our observations too demonstrate, when HCur is dissolved in aqueous buffer or in cellular media its absorbance decreases gradually.^{12, 18} There is however, no interference to the absorbance of HCur from any of the species generated from it (as all are colourless). Breakdown of curcumin is clearly evident as a gradual decline in absorbance when dissolved either in aqueous buffer or in cellular media.^{12,18} To better comprehend situations and interpret pharmacological properties, it is important to have curcumin in solution as a "single unit" that entails preventing its degradation



before interaction with a biological target. Formation of a coordination compound with it can accomplish this.^{12,13,18,20} Metal-bound curcumin exists as a "single-unit".^{12,13,18,20} Inclusion of a metal ion should also aid cellular uptake and take care of aspects related to solubility.²¹

We synthesized a coordination complex (Zn^{II} -HCur) keeping these facts in mind. The complex was found to be stable in aqueous solution and in biological cellular media indicating HCur bound to Zn^{II} remains a "single-unit". By observing changes in absorption and emission spectra pertaining to Zn^{II} -HCur, interaction with calf-thymus DNA was experimentally explored, something not possible with HCur for reasons mentioned earlier (Fig S1, SI). A comprehensive *in silico* analysis was performed to realize nature of binding of HCur and to confirm and support what could have been achieved experimentally had HCur not degraded in solution.^{12,13,18,20} To this end, molecular docking and molecular dynamics simulation techniques were used.^{22, 23} Molecular docking provides three-dimensional structures of compounds bound to DNA.²⁴⁻²⁷ It generates a reasonably good understanding between experimental and theoretical approaches. Using molecular dynamics simulation we were able to gain in-depth understanding of binding pattern and in the process pinpoint key structural characteristics of generated "DNA-compound" adducts.²⁴⁻³¹

2. Experimental

2.1 Materials

2.1.1 Chemicals

HCur was purchased from Sigma-Aldrich and stored in the dark following its dissolution in methanol. DNA extracted from thymus of a calf was bought from Sisco Research Laboratories, India and dissolved in millipore water containing 120 mM NaCl, 35 mM KCl and 5 mM CaCl_2 . By measuring absorbance at 260 nm and considering molar extinction coefficient for DNA as



6600 M⁻¹ cm⁻¹, its concentration was ascertained. Absorption at 260 and 280 nm respectively, helped in determining whether the DNA was adequately free of protein, to decide if it required further purification. In order to further analyse the calf thymus DNA we would use, a CD spectropolarimeter was employed to procure a CD spectrum at 260 nm (J815, JASCO, Japan). Zinc(II)-acetate was bought from Sigma-Aldrich. Sodium nitrate (AR), sodium dihydrogen phosphate and disodium hydrogen phosphate were obtained from E Merck, India. All solutions were prepared in millipore water.

2.2 Instruments used:

All spectroscopy related experiments were performed on a JASCO V-630 spectrophotometer, Japan. Temperature was controlled using a circulating thermo-stated water bath. Fluorescence measurements were made on Duetta, Horiba Scientific. CD was recorded on J815 Spectropolarimeter, JASCO, Japan. IR of solid samples were recorded on Spectrum Two, FTIR spectrophotometer, Perkin Elmer in the range 4000-400 cm⁻¹. TGA was done on Mettler Toledo TGA/SDTA 851 thermal analyzer. Micromass Q-T of microTM, Waters Corporation was used to record mass spectrum. pH of solutions were recorded on a pH meter (LI 613, Elico, India). DFT, molecular docking and molecular dynamics simulation were performed on a Linux operating system supported with GPU-NVIDIA RTX 3060 Ti and Intel i7 9700kF processor.

2.3 Methods

2.3.1 Preparation of Zn^{II} Curcumin [Zn(Cur)]

HCur (0.74 g, 2 mmole) was dissolved in 50 mL de-aerated acetonitrile-methanol mixture (1:3). The solution was neutralized with triethylamine (0.277 mL, 2 mmole) followed by addition of Zn(CH₃COO)₂ (0.37g, 2 mmole) dissolved in 30 mL de-aerated methanol-water mixture (1:1). Argon gas was passed through the mixture to maintain an inert atmosphere. The



mixture was stirred under heat ($\sim 60^{\circ}\text{C}$) for an hour. It was then refluxed for another 2 hours under inert atmosphere. An orange brown precipitate was obtained. It was recovered and washed with chloroform, diethyl ether, ethanol, THF and acetonitrile separately, depending on solubility of HCur in these solvents to wash away undesired impurities. A pure coordination compound was obtained which was not soluble in common solvents like methanol, ethanol, acetonitrile or dichloromethane. However, it was partly soluble in dimethylformamide (DMF) and to a reasonably good extent in dimethyl sulphoxide (DMSO).

2.3.2 Quantum Chemical Calculations:

2.3.2.1 Perspective:

Despite our best efforts, since we were unable to procure single crystals of $[\text{Zn}(\text{Cur})]$ a structure indicating its coordination environment eluded us. Again, due to its amorphous nature we were unable to solve its structure using powder X-ray diffraction data we collected. Hence, we were compelled to rely on data obtained from spectroscopic measurements that enabled us to create a model for the coordination environment around Zn^{II} . Subsequently, this model was improved by theoretically calculating its UV-vis absorption spectrum and comparing it with that obtained experimentally.

2.3.2.2 Computational Methodology

All computations were carried out using DFT method and Gaussian 09 programme.³² For C, H and O we used standard 6-31G+(d,p) basis set coupled with Becke three parameter hybrid functional and Lee-Yang-gradient Parr's corrected correlation functional (B3LYP).³³ For Zn, the LanL2DZ basis set was used.³⁴ To account for long-range dispersion impact, Becke-Johnson damping (GD3BJ) and Grimmes' third order correction for dispersion were used. In both gaseous and DMSO solvent environments, ground state (S_0) geometries were fully



optimised utilizing the program's extremely strict convergence criteria. In order to guarantee the stationary points' global minima, frequencies were calculated on optimized geometries where all vibrational frequencies were found to be positive. All simulations regarding solution phase were performed in DMSO as solvent using integral equation formalism variant (IEFPCM) of polarizable continuum model.³⁵ TDDFT in DMSO solvent was carried out to establish the geometry of the coordination compound.³⁶ Frontier MO composition analysis was performed with Gauss Sum programme³⁷ and investigations of MO orbital and molecular electrostatic potential (MEP) surface were done with GaussView. In addition, frontier molecular orbital energies were used to calculate quantum mechanical descriptors, like MO gap (E), ionization potential (IP), electron affinity (EA), electronegativity (χ), chemical hardness (η), mean energy (M), chemical potential (μ), chemical softness (σ) and electrophilicity index (ω). These computations were performed using the following formulae.³⁸

$$\Delta E = E_{\text{LUMO}} - E_{\text{HOMO}} \quad (1) ; \quad \text{IP} = -E_{\text{HOMO}} \quad (2)$$

$$\text{EA} = -E_{\text{LUMO}} \quad (3) ; \quad \chi = -\mu = (\text{IP} + \text{EA})/2 \quad (4)$$

$$\eta = \Delta E/2 \quad (5) ; \quad \sigma = 1/2\eta \quad (6)$$

$$\omega = \chi^2/2\eta \quad (7) ; \quad \text{M} = -\chi \quad (8)$$

2.3.2.3 Non-covalent interaction (NCI) and bond critical point analysis:

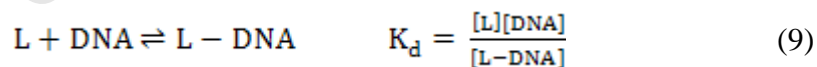
This study was carried out to separate attractive and repulsive interactions present in molecular systems allowing us to observe non-covalent interactions by mapping them as iso-surfaces over the molecular system.³⁹ It is possible to differentiate between attractive/stabilizing (favorable) and repulsive (unfavorable) interactions using the plot of reduced density gradient (RDG) versus sign of the product of second Hessian eigenvalue and electron density [sign (λ_2) pin a.u.]. The color scheme of red, green and blue depicts strength of interactions; blue iso-surface denote



strong attractive interactions, red iso-surface, strong repulsive interactions and green iso-surface, weak attractive interactions. As expected, covalent and coordination bonds are represented by blue. NCI calculations were done on Multiwfn version 3.8.⁴⁰ The RDG-based NCI spike and iso-surface plot of [Zn(Cur)] in gaseous and solution phase were visualized using VMD 1.9.2 program. In addition to electron density, at bond critical points it helps us to characterize the strength of hydrogen bonds by DAMQT-2.1.0 package.⁴¹

2.3.3 Interaction of [Zn(Cur)] with calf thymus DNA:

As already mentioned, HCur dissolved in phosphate buffer shows gradual decrease in absorbance (Fig. S1, SI) that is realized by monitoring it with time.^{12, 18} For this reason, DNA binding studies could not be performed with it as the compound degrades in solution. For this reason, an attempt was made to follow the interaction theoretically to realize what could have happened if HCur were present as one unit and were to interact with DNA. On the other hand, [Zn(Cur)] dissolved in 150 mM NaCl, 25 mM KCl and 5 mM CaCl₂, in phosphate buffer (pH 7.4) or in biological milieu is stable and does not degrade (Fig. S1, S I). Hence, titration of [Zn(Cur)] with calf thymus DNA has been possible. A change in absorbance or fluorescence following addition of calf thymus was monitored. The following equilibrium (Eq. 9) depicts binding of [Zn(Cur)] with calf thymus DNA.



L represents [Zn(Cur)]. Reciprocal of K_d provides the apparent binding constant (K_{app}).⁴²⁻⁴⁶

2.3.3.1 By UV-Vis spectroscopy

Eq. 10 may be generated from Eq. 9 where reciprocal of the change in absorbance was plotted against reciprocal of $(C_D - C_0)$. C_D denotes total concentration of calf thymus DNA while C_0 ,



denotes concentration of [Zn(Cur)]. Using Eq. 10, ΔA_{\max} and $K_{\text{app}} (= K_d^{-1})$ was determined from the intercept and the slope respectively.

$$\frac{1}{\Delta A} = \frac{1}{\Delta A_{\max}} + \frac{K_d}{\Delta A_{\max}(C_D - C_0)} \quad (10)$$

ΔA denotes change in absorbance of [Zn(Cur)] at pH = 7.4. ΔA_{\max} indicates the maximum possible change in absorbance.

$$K_d = \frac{\left[C_0 - \left(\frac{\Delta A}{\Delta A_{\max}} \right) C_0 \right] \left[C_D - \left(\frac{\Delta A}{\Delta A_{\max}} \right) C_0 \right]}{\left(\frac{\Delta A}{\Delta A_{\max}} \right) C_0} \quad (11)$$

$$C_0 \left(\frac{\Delta A}{\Delta A_{\max}} \right)^2 - (C_0 + C_D + K_d) \left(\frac{\Delta A}{\Delta A_{\max}} \right) + C_D = 0 \quad (12)$$

Subsequently, $\Delta A/\Delta A_{\max}$ was plotted against C_D . Eqs. 11 & 12 were used to fit the experimental data by non-linear square fit analysis that provided a value for apparent binding constant for the interaction of [Zn(Cur)] with calf thymus DNA.⁴²⁻⁴⁶ A plot of $\Delta A/\Delta A_{\max}$ against ratio of concentration of calf thymus DNA to [Zn(Cur)] provides two straight lines intersection of which provides n_b (number of nucleotides bound to [Zn(Cur)]). Apparent binding constants (K_{app}) obtained from Eqs. 10 & 12 when multiplied with n_b provides the overall binding constant (K^*). The titrimetric data on [Zn(Cur)] with calf thymus DNA was also analyzed according to a modified form of the Scatchard equation [Eq. 13].⁴⁷ Overall binding constant (K^*) and site size n ($= n_b^{-1}$ = number of bound complex per nucleotide) was determined.

$$r/C_f = K^*(n - r) \quad (13)$$

$r = C_b/C_D$; C_b denotes concentration of bound form of [Zn(Cur)] while C_f denotes free form.



2.3.3.2 By Fluorescence spectroscopy

Binding of [Zn(Cur)] with calf thymus DNA was also followed by fluorescence spectroscopy. [Zn(Cur)] was excited at 436 nm while emission was followed over the wavelength range 436 to 700 nm. Emission maxima appeared at 584 nm. Upon addition of calf thymus DNA, fluorescence increased which was followed after allowing for suitable corrections owing to dilution; thus ΔF was obtained. Like the monitoring by UV-Vis spectroscopy, standard equations (Eqs. 10-13) were used where change in fluorescence (ΔF) was considered instead of change in absorbance (ΔA) and plotted against change in concentration due to DNA and [Zn(Cur)]. Hence, using fluorescence spectroscopy, apparent binding constant (K_{app}), overall binding constant (K^*) and site size of interaction (either n_b or n) were determined.

2.3.4 Molecular Modelling

2.3.4.1 Molecular Docking

Molecular docking studies were performed using the Autodock software (version 4.2.6) which is an interactive molecular graphics program using which the binding energy was obtained.⁴⁸ Additionally, the command-line tool Autodock Vina (version 1.2.3; <http://vina.scripps.edu>)^{48,49} was used from where binding affinity values were obtained. Both binding energy and binding affinity, output of programs used and regarded as docking score were generated using different scoring functions.^{50,51} The crystal structure of DNA (PDB ID: 1BNA)⁵² was downloaded from the protein data bank (<http://www.rcsb.org/pdb>) having resolution of 1.90Å. The downloaded DNA has A and B chains having the sequence 5'-D(CGCGAATTCGCG)-3'. Before performing molecular interaction studies DNA was checked for missing nitrogenous base pairs using UCSF Chimera (version 1.15; <https://www.rbvi.ucsf.edu/chimera>) and its energy was minimized using



steepest descent and conjugate gradient techniques. It was then saved in PDB format. Subsequently, molecular interaction experiments were performed. Optimized HCur and [Zn(Cur)] were saved as two separate mol2 files and were further converted to PDB using the openbabel software. Thereafter, using Autodock tools (version 1.5.6) saved PDB files of DNA and chosen molecules were opened. After merging non-polar hydrogens on both receptor and target molecules they were saved in PDBQT format.⁵³ Grid boxes were created with specific dimensions at a spacing of 0.35 Å. Docking studies of 1BNA-HCur and 1BNA-[Zn(Cur)] were carried out using Lamarckian Genetic Algorithm (LGA) to achieve the lowest free energy of binding (G). For molecular docking studies, three replicates were performed; for each a total number of 10 solutions were computed, each showing an energy minima having a population size of 150 and number of evaluations ~250000, the maximum number of generations being 27000.^{53, 54} After docking, RMSD cluster maps were obtained with cluster tolerance of 2.0 Å, each for HCur and [Zn(Cur)]. The BIOVIA Discovery Studio (version 2021) and PyMOL software (DeLano, 2002) were used for visualisation of 2D and 3D interactions of different nucleotides with HCur and [Zn(Cur)], to visualize the best possible geometry of compounds inside DNA.

2.3.6.2 Molecular Dynamics

MD simulation studies were carried out on free DNA (PDBID: 1BNA), HCur docked DNA and [Zn(Cur)] docked DNA complex to investigate stability and physical movements. Desmond (version 2020.1)⁵⁵ was used to run molecular dynamics simulation which is a GPU-accelerated program running on the Linux operating system integrated with an NVIDIA RTX 3060 Ti GPU and Intel i7 9700kF processor. In order to prepare the systems, the OPLS-2005 force field⁵⁶ and explicit solvent model with SPC water molecules were employed.⁵⁷ Energy of all systems were



then reduced by using an orthorhombic boundary solvation box having dimension $10\text{\AA} \times 10\text{\AA} \times 10\text{\AA}$. Then, the correct quantity of Na^+ or Cl^- ions was introduced to each system to neutralize it. Each system received an additional 0.15 M NaCl solution to replicate the physiological environment. The Desmond default relaxation approach was used to relax the prepared systems. An NVT ensemble was initially used to equilibrate the entire system for 500 ps at 10 K. Following the preceding phase, an NPT ensemble was used to complete a quick run of equilibration and minimization for 100 ns at 300 K and 1.01325 bar pressure. The Nose-Hoover chain coupling approach was used to set up NPT ensemble.⁵⁸ Temperature was set to 300 K, relaxation period was set at 1.0 ps and pressure was maintained at 1 bar throughout simulations. A time step of 2 fs was applied. With a relaxation duration of 2 ps, the Martyna-Tobias-Klein chain coupling scheme barostat method was employed to control pressure.⁵⁹ Long-range electrostatic interactions were calculated using the particle mesh Ewald approach⁶⁰ with a fixed coulomb interaction radius of 9.0\AA . With each trajectory, bonded forces were calculated using RESPA integrator for a time step of 2 fs. Maestro, a Desmond GUI application, was used to study simulation interaction diagrams. One can also forecast stability of DNA and DNA-ligand compounds using simulation-derived parameters including root-mean square deviation (RMSD), root mean square fluctuation (RMSF), number of H-bonds and radius of gyration.⁶¹

2.3.6.3 Binding free energy analysis by MDS

The generalized Born surface area (MM-GBSA) method and molecular mechanics were utilized to calculate binding free energies of DNA-ligand complexes. The simulation trajectory's last 10 frames out of 1000 with a 1-step sampling size and OPLS-2005 force field coupled with python script `thermal_mmgbsa.py` were used to determine MM-GBSA binding free energy.^{62, 63} The principle of additivity was used to estimate binding free energy of MD trajectory using MM-



GBSA (kcal/mol), in which individual energy modules like columbic, covalent, hydrogen bond, van der Waals, self-contact, lipophilic, solvation and stacking of ligand and DNA were obtained. Equation 14 was used to calculate $\Delta G_{\text{binding}}$

$$\Delta G_{\text{binding}} = \Delta G_{\text{MM}} + \Delta G_{\text{Solv}} - \Delta G_{\text{SA}} \quad (14)$$

where $\Delta G_{\text{binding}}$ designates binding free energy, ΔG_{MM} designates difference between free energies of DNA-ligand complexes and total energy of DNA and ligand in an isolated state, ΔG_{solv} denotes difference in solvation energies of the DNA-ligand adduct and sum of the solvation energies of DNA and ligand in unbound state, ΔG_{SA} designates difference in surface area energies for DNA and ligand.

3. Results and Discussions

3.1 Characterization of the Zn^{II}-Curcumin complex

3.1.1 Using different instrumental techniques:

Owing to poor solubility in water, spectrum of [Zn(Cur)] was recorded in DMSO (Fig. S2, SI). λ_{max} was detected at 426 nm. IR spectrum of [Zn(Cur)] was compared with that of HCur (Fig. S3 and S4, S I respectively). Mass spectrum of [Zn(Cur)] shows molecular ion peaks at $m/z = 508.4731, 510.5261, 512.2132$ owing to three relatively abundant isotopes of Zn (m/z_{theo} being 508.38 for ⁶⁴Zn; 510.38 for ⁶⁶Zn; 512.38 for ⁶⁸Zn) (Fig. S5, SI). Following the loss of a molecule of water from the molecular ion, peaks with m/z values 490.7648, 492 and 494 were obtained, Fig. S5, SI; m/z_{theo} for these fragments being 490.38 for ⁶⁴Zn; 492.38 for ⁶⁶Zn; 494.38 for ⁶⁸Zn. Loss of a molecule of water and acetate from the molecular ion, results in peaks with m/z values 449.2687, 451.4157 and 453.1284; Fig. S5, SI; m/z_{theo} being 449.38 for ⁶⁴Zn; 451.38 for ⁶⁶Zn; 453.38 for ⁶⁸Zn. Experimental responses in the mass spectrum were in excellent agreement with theoretically expected fragments. In fact, they were also in extremely good agreement pertaining



to that expected of a fragment considering the relative abundance of isotopes of Zn [five stable isotopes being ^{64}Zn (48.63%), ^{66}Zn (27.90%), ^{67}Zn (4.10%), ^{68}Zn (18.75%), and ^{70}Zn (0.62%); the three most abundant of the five were identified in our mass spectrum]. Hence, mass spectrum provides clean evidence in favor of $[\text{Zn}(\text{Cur})(\text{CH}_3\text{COO})\text{H}_2\text{O}]$. TGA (Fig. S6, SI) also indicates that formula of our coordination compound is $[\text{Zn}(\text{Cur})(\text{CH}_3\text{COO})\text{H}_2\text{O}]$.

3.1.2 DFT calculations based on spectroscopic evidence

Ground states of optimized molecular structures were singlet. The ground state optimized geometries of $[\text{Zn}(\text{Cur})]$ (in gaseous state and in DMSO) and of Cur in keto and enol forms are depicted in Figs. 3(A) and 3(B) respectively, with a numbering scheme for the coordination environment. The optimized coordinates of these configurations $[\text{Zn}(\text{Cur})]$ are provided in Table S1, SI. Important parameters concerning the coordination geometry are arranged in Table 1. Calculated bond lengths (Table 1) for Zn–O are in good agreement with those that are reported for $[\text{Zn}(\text{Cur})(\text{bipy})(\text{acetate})]$,⁶⁴ whose structure was established from single crystal X ray diffraction studies. Final optimized structures of ground state configurations show tetrahedral coordination both in gas and solution (DMSO) phases (Fig. 3A).

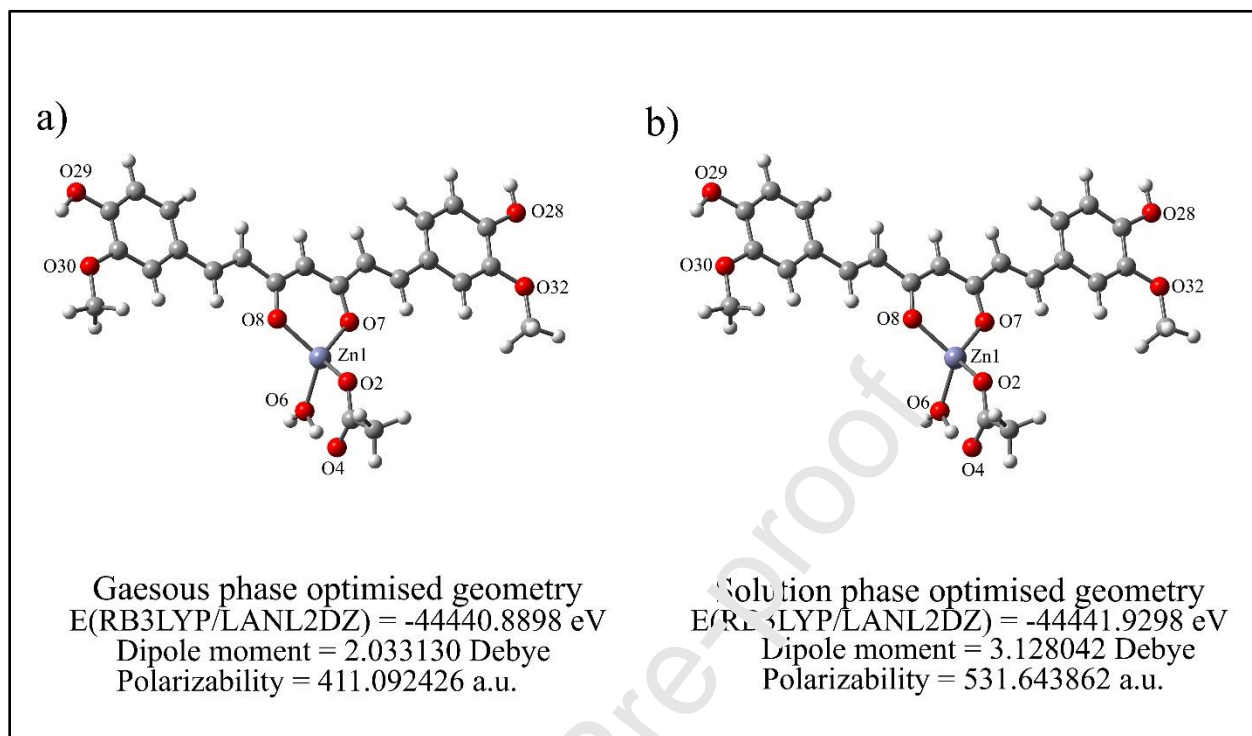


Fig 3A: Ground state optimized geometries of the [Zn(Cur)] (a) Gaseous phase (b) Solution phase

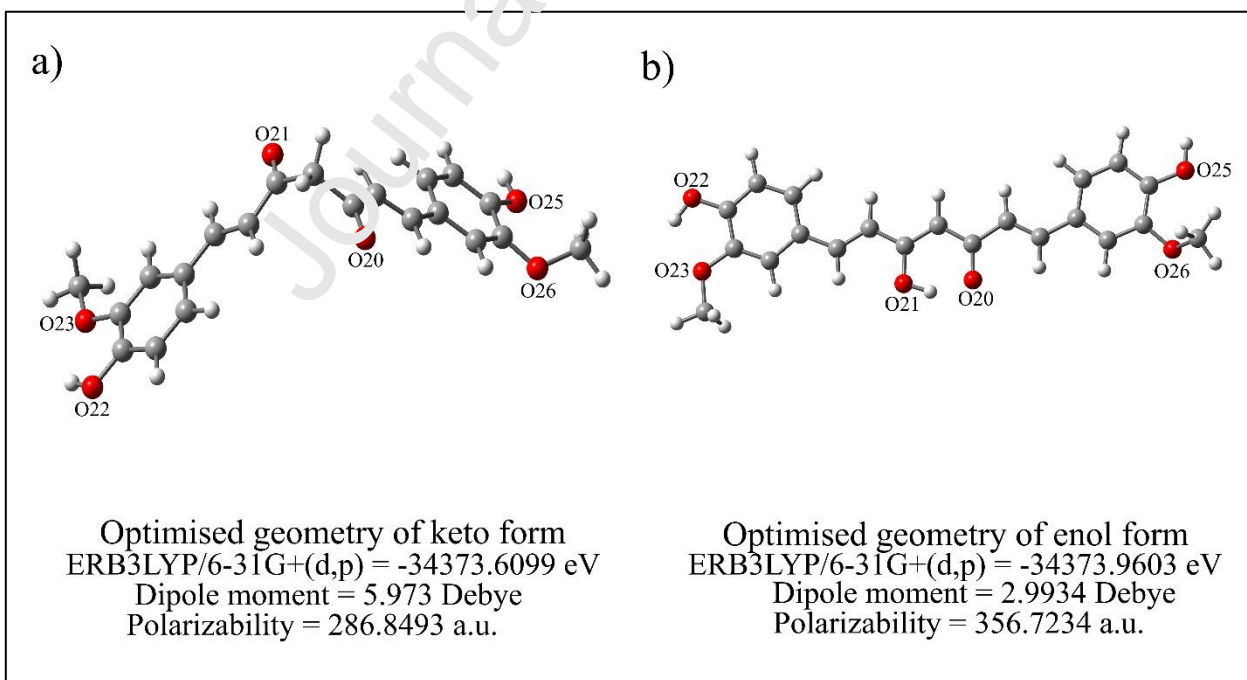


Fig 3B: Ground state optimized geometries of the HCur (a) keto form (b) enol form

Table 1: Coordinated bond distances (in Å) and bond angles (in °) of [Zn(Cur)]

Bond	Gaseous phase	In DMSO	Angle	Gaseous phase	In DMSO
Zn1–O2	1.976	2.006	O2–Zn1–O6	92.08	90.55
Zn1–O7	1.967	1.987	O2–Zn1–O7	120.43	106.36
Zn1–O6	1.993	2.008	O6–Zn1–O8	117.50	107.79
Zn1–O8	1.968	1.989	O7–Zn1–O8	91.66	90.77

3.1.2.1 MO composition analysis:

The frontier orbital of [Zn(Cur)] optimized in gas and solution phases and HCur in solution phase are shown in Fig. S6 and Fig. S7, SI, respectively. Description of both occupied and virtual MOs were made based on their atomic composition and visual inspection of a three-dimensional representation. [Zn(Cur)] moiety was assumed to be composed of four fragments, Zn, Curcumin, water and acetate. Their compositions are described in Table S2, SI. We observed both for gas and solution phases optimized geometries, HOMO-1 to LUMO+4 have no contribution from the metal; i.e. contributions only from curcumin. For HOMO-2 to HOMO-4 there was some contribution from the metal. According to calculations, the HOMO-LUMO energy gap for [Zn(Cur)] in gas and solution phases were 3.09 eV and 2.63 eV respectively. On the other hand, HOMO-LUMO energy gap for HCur in solution phase was 3.30 eV (shown in Fig. S8, SI). The HOMO-LUMO gap in gas and solution phases of [Zn(Cur)] are shown in Figure 4.

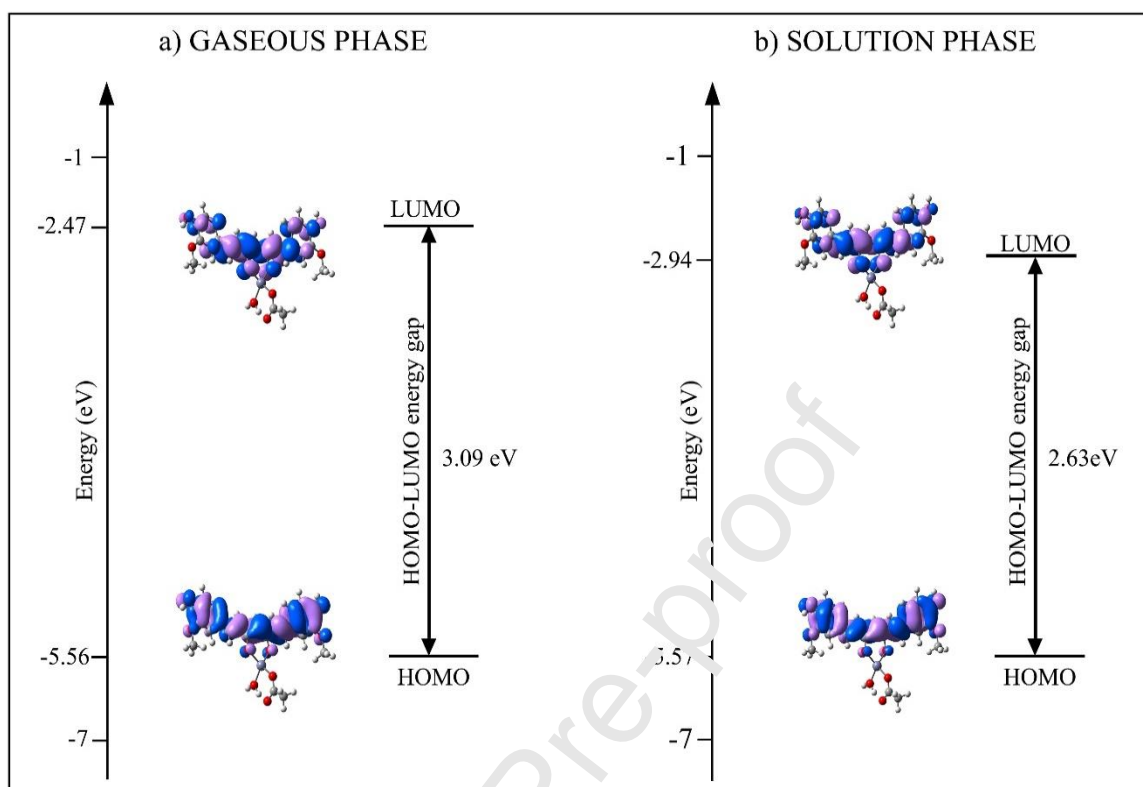


Fig. 4: HOMO-LUMO gap of [Zn(Cur)] (a) Gas phase (b) Solution phase

The highest occupied molecular orbital (HOMO) and lowest unoccupied molecular orbital (LUMO) are ligand-centric in each phase with almost the entire contribution coming from HCur. For molecular crystals, optical energy band gap resulting from UV-Vis absorption could be used to confirm the HOMO-LUMO energy gap (Fig. 4). The optical energy band gap (E_g) calculated using $E_g = 1240/\lambda_{\max}$ eV was found to be 2.91 eV equivalent to theoretical HOMO-LUMO energy gap of [Zn(Cur)] in DMSO (2.63 eV).

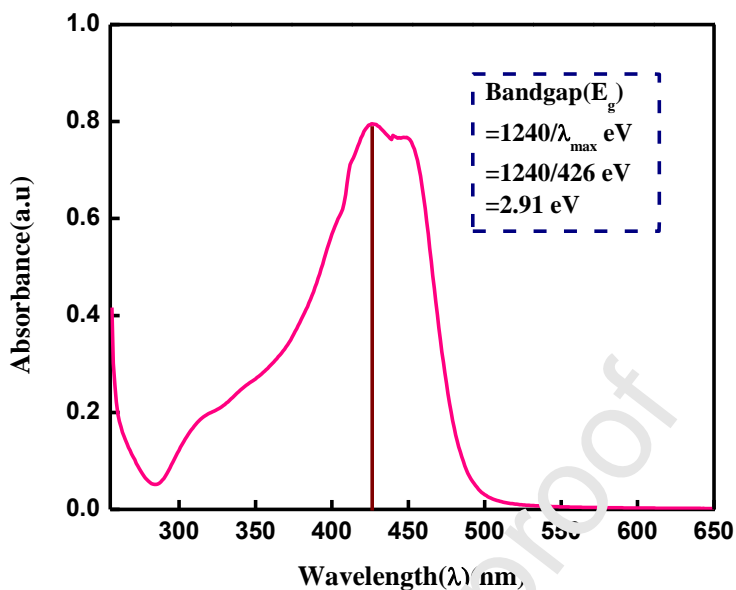


Fig. 5 Experimental UV-Vis absorption maxima with corresponding optical bandgap

3.1.2.2 Opto-electronic absorption property

Since excitation from ground state to an excited state in a dielectric medium (DMSO) would result in identical absorption as that recorded experimentally in the same solvent, opto-electronic property was helpful in pinpointing precise molecular geometry. DMSO has a cut off wavelength for absorption at ~ 268 nm. Since the absorption spectrum of [Zn(Cur)] exhibits dispersion below 300 nm, therefore to compare observed patterns with calculated ones, the spectrum was recorded up to 650 nm rather than going below 300 nm (Fig. 5). A multiple transition nature for [Zn(Cur)] is supported by computed electronic absorption spectrum in DMSO having several peaks. The experimental spectrum's peaks were visually assigned. In Table S3, SI, the most likely transitions are presented in increasing order of energy in which they appear in the spectrum with maximum intensity ($f \geq 0.10$) corresponding to experimental absorption peaks and related excitation wavelengths, energy, oscillator strengths (f), character

and CI coefficients. Excitation peaks were mainly due to charge-transfer transitions within HCur. Almost all states were regarded as singlet that were used for TDDFT calculations.

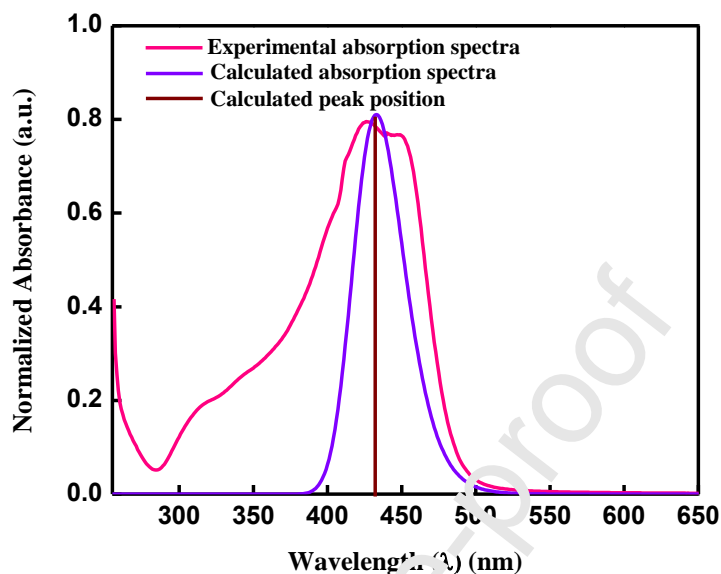


Fig. 5: Comparison of experimental and theoretical UV-Vis absorption spectra showing most feasible peak positions

Natural transition orbital (NTO) analysis based on computed transition density matrices were used to explain results of excited state computation. The terms "electron/particle" and "hole" transition orbitals were used to describe virtual/unoccupied and occupied NTOs respectively. From a relative weightage of transition density matrices and occupied-virtual pair contributions to excitation we were able to recognize and depict electronic transitions that were being studied in terms of excitation from a hole-NTO to an electron-NTO for solution phase excited geometry. Fig. 6 shows NTOs for the most significant peaks.

The most significant computed peak was at 431 nm (2.7313 eV, $f = 1.6121$), which was the lowest energy transition observed experimentally, close to 426 nm. This transition is due to ILCT. The next higher energy UV transition estimated at 394.88 nm (3.13 eV, $f = 0.180$) is

also attributed to ILCT and was experimentally found at 410 nm. The UV excitation at 351.07 nm (3.5316 eV, $f = 0.0001$) detected close to the experimental peak at 350 nm may be attributed to ILCT or an extremely weak LLCT.

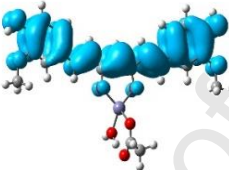
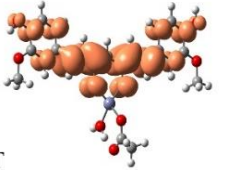
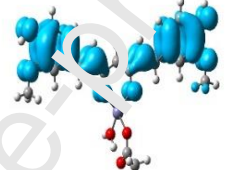
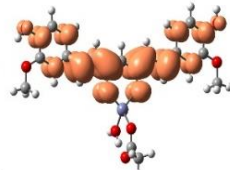

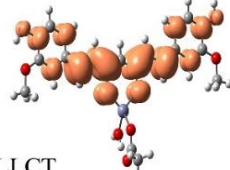
Experimental Excitation (nm)	Calculated Excitation (nm)	Excitation Energy (eV)	Excited state involved	Osc. Strength (f)	λ_i	ELECTRON	HOLE
426	453.94	2.7313	S3	1.6121	1		
						ILCT	
410	394.88	3.1398	S5	0.1080	0.97		
						ILCT	
350	351.07	3.5316	S6	0.0001	0.98		
						ILCT/LLCT	

Fig. 6: NTO analysis describing the calculated UV-Vis peak positions

3.1.2.3 Quantum descriptor analysis:

Frontier molecular orbitals affect a molecule's kinetic stability, electrical conductivity and chemical reactivity (HOMOs and LUMOs). Soft molecules are those that have narrow HOMO-LUMO energy gap. These exhibit greater biological and chemical reactivity. Molecules having large HOMO-LUMO energy gap have low biological response, are extremely stable and are less reactive towards other compounds. Intra-molecular charge transfer (ICT) from an electron-donor group to an electron-acceptor group is possible in small HOMO-LUMO energy gaps. Good



electron acceptor molecular systems have lower E_{LUMO} than good electron donor molecular systems with higher E_{HOMO} . In Table 2, we compare the quantum descriptor of HCur with that of [Zn(Cur)] that was obtained after geometry optimisation. Electron donation (IP) and electron acceptance (EA) is facilitated due to low HOMO-LUMO gap. Electron affinity of [Zn(Cur)] is quite high compared to HCur which indicates that the complex might easily interact with nucleotides from DNA by dragging the electron density towards itself. On the other hand, a soft molecule is defined as one having lower η value (Eq. 5).^{65, 66} Upon complex formation with Zn^{II} , HCur becomes soft and shows greater electron delocalization that facilitates more non-covalent interaction. A high value of ω (electrophilicity index) represents high affinity towards electron rich species. [Zn(Cur)] has a higher affinity compared to HCur.

Table 2: Quantum descriptor for HCur and [Zn(Cur)] in eV with B3LYP-6-31G+(d,p) functional

Compound	HOMO	LUMO	ΔE	IP	EA	X	η	M	σ	ω
HCur	-5.57	-2.27	3.30	5.57	2.27	3.92	1.65	-3.92	0.60	4.65
[Zn(Cur)]	-5.57	-2.94	2.63	5.57	2.94	4.26	1.32	-4.26	0.75	6.87

3.1.2.4 MEP surface analysis:

Fig 7 displays “molecular electrostatic potential surface” computed over optimal geometries in both gas and solvent phases. The envelope's iso-value was selected to be 0.02 a.u. and the reverse rainbow color scheme was used throughout.⁶⁷ Areas with negative potential are denoted in red, while areas with positive potential are in blue. It is evident hydrogen atoms on phenolic O-H are positively charged, whereas hydrogen on CH_3 are just marginally positive. H- atoms in H_2O are likewise identified to be somewhat positive. The most negative potential regions were next to carbonyl O atoms, along with O-atoms of acetate, while the ring of HCur was found to have greater MEP values than carbonyl oxygens. Inferring that there is a strong likelihood that



molecules would create hydrogen bonding connections between H of water and carbonyl O of an acetate that could eventually stabilize the system, we compared MEP of keto and enol forms of HCur only and found carbonyl oxygens are electron rich (red in colour, Fig. S9, SI) along with phenolic OH.

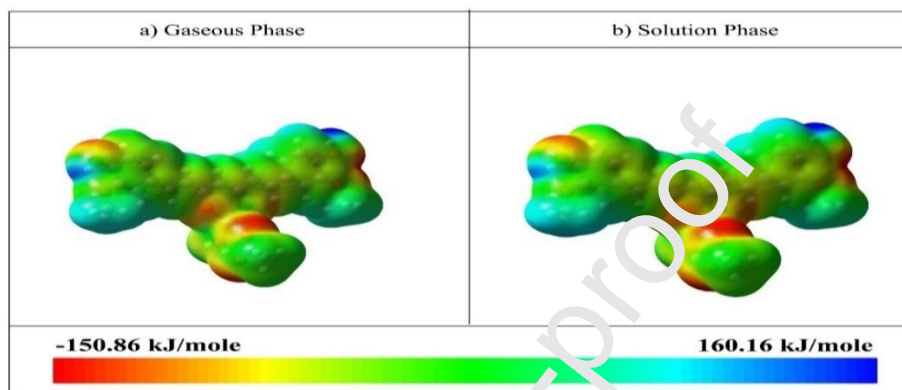


Fig 7: Molecular electrostatic Potential surface of [Zn(Cur)] in (a) Gas phase and (b) solution phase

3.2 Non-covalent interactions (NCI) and bond Critical Point Analysis

From NCI analysis (Fig. 8), it was observed carbonyl-O of acetate in [Zn(Cur)] and H of H-O-H in water form strong intra-molecular hydrogen bond; displayed as the blue iso-surface.

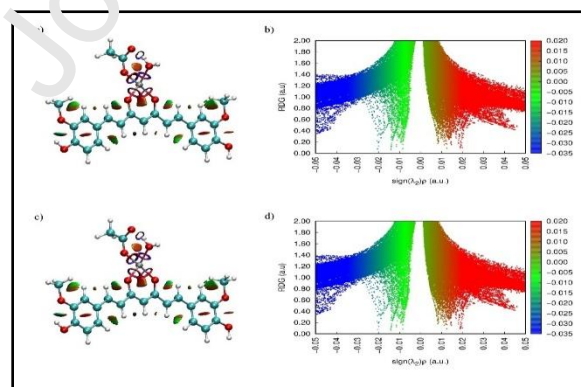


Fig 8: NCI plots of [Zn(Cur)] (I) Gas phase (a,b), (II) Solution Phase (c, d)

The bond strength of [Zn(Cur)] was estimated by critical point analysis with Quantum theory of atoms-in-molecules (QTAIM) descriptors. Surprisingly, there is a strong hydrogen bond obtained between water and acetate ion. Using critical point analysis, we observed threefold enhancement in strength of the formed hydrogen bond over that of normal hydrogen bond. It may be noticed from Table S4, SI that for normal hydrogen bonds (NHB) $\rho = 0.02 \text{ e/bohr}^3$ and for strong hydrogen bonds it is (SHB) $\rho = 0.062 \text{ e/bohr}^3$. In fact, strength of an SHB is equivalent to that of a coordinate covalent bond, but less than a covalent bond which is usually 0.2 e/bohr^3 .

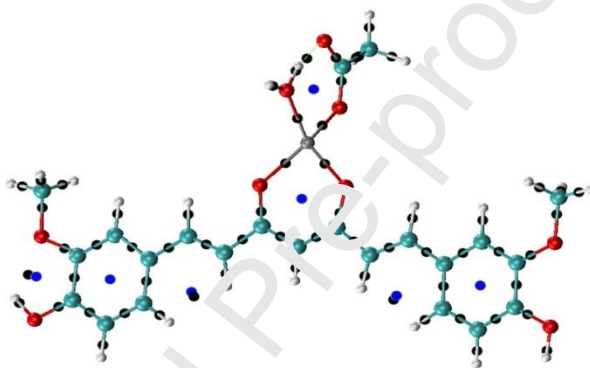
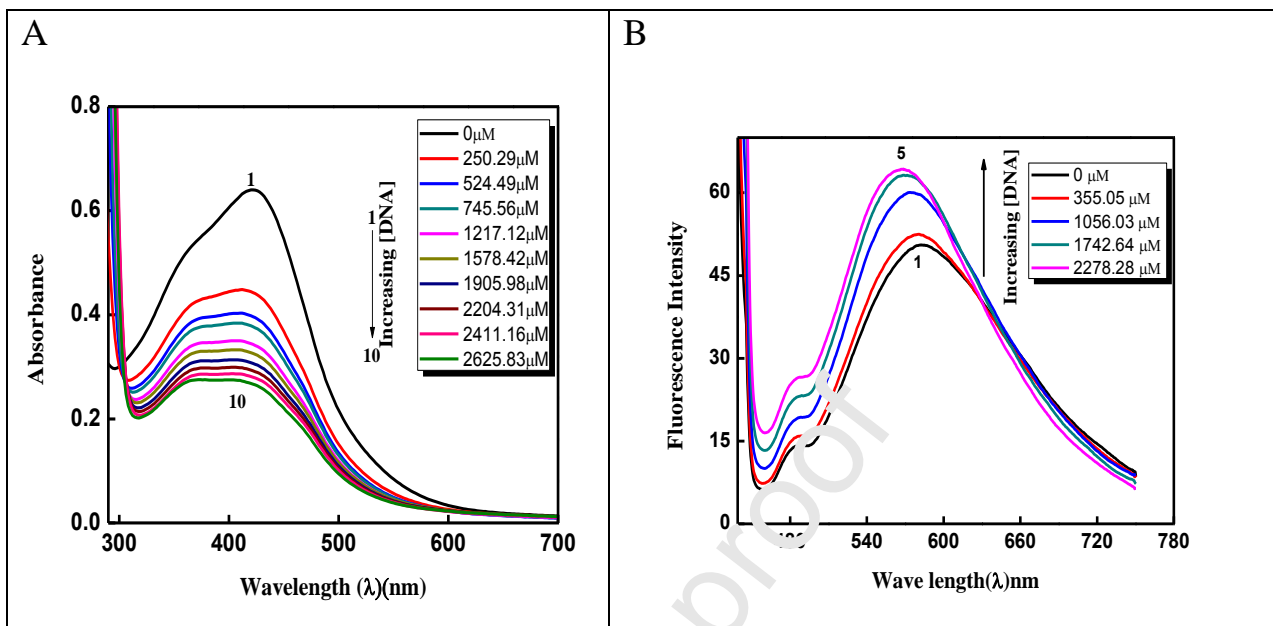


Fig 9: DFT optimised geometry of [Zn(Cur)] showing hydrogen bond critical points (CP) indicated by blue and black spheres; black spheres represent bond critical points (3, -1) in which one of them represents hydrogen bond critical point; blue spheres represent ring critical point.

3.3.1 Experimental binding of [Zn(Cur)] with calf thymus DNA

[Zn(Cur)] was titrated with calf thymus DNA at constant pH (= 7.4) and constant ionic strength (0.15 mM) of the medium. A gradual decrease in absorbance at 430 nm or a gradual increase in fluorescence at 570 nm helped in evaluating the interaction occurring between [Zn(Cur)] and calf thymus DNA (Fig. 8).

Fig. 9: (A) Absorption spectra of [Zn(Cur)] in the absence (1) and presence of different

concentrations of calf thymus DNA (2) 250.29 μM , (3) 524.49 μM , (4) 745.56 μM , (5) 1217.12 μM , (6) 1578.42 μM , (7) 1905.98 μM , (8) 2204.31 μM , (9) 2411.16 μM and (10) 2625.83 μM ; [NaCl] = 150 mM, pH = 7.4; Temp. = 298 K. (B) Fluorescence intensity of [Zn(Cur)] in the absence (1) and presence of different concentrations of calf-thymus DNA (2) 355.05 μM , (3) 1056.03 μM , (4) 1742.64 μM , (5) 2278.28 μM ; [NaCl] = 150 mM, pH = 7.4; Temp. = 298 K.

Fig. 9 is a double reciprocal plot of $1/\Delta A$ versus $1/[C_D - C_L]$ [Eq. 10] that provides values for K_{app} ($= K_d^{-1}$) from two independent titrations.⁴²⁻⁴⁶ An average of their values was $2.23 \times 10^3 \text{ M}^{-1}$.

Fig. 10 B is a plot of $\Delta A/\Delta A_{\text{max}}$ versus concentration of calf thymus DNA to which non-linear curve fit was applied (Eqs. 11 & 12). Two independent titrations provide an average apparent binding constant of $2.25 \times 10^3 \text{ M}^{-1}$ at 298 K. Inset of Fig. 10 provides a value of n_b as 10.0, i.e. number of nucleotides bound to [Zn(Cur)] following interaction with calf thymus DNA.⁴²⁻⁴⁶

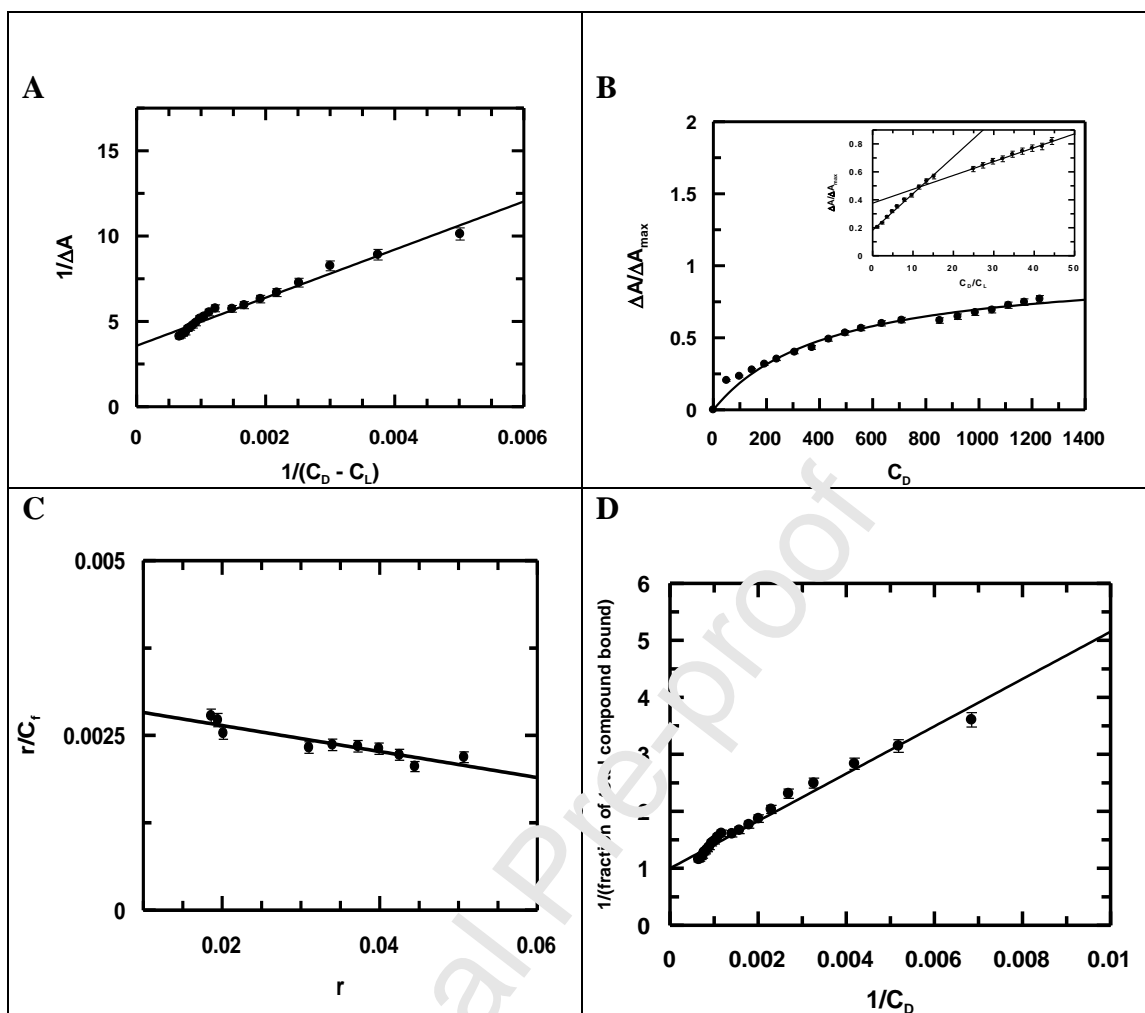


Fig 10: (A) Double reciprocal plot for the interaction of [Zn(Cur)] with calf-thymus DNA to evaluate apparent binding constant (K_{app}) of the complex to DNA, (B) binding isotherm for [Zn(Cur)] interacting with calf thymus DNA when $\Delta A/\Delta A_{max}$ was plotted against concentration of DNA; the dark line is the fitted data obeying Eq. 12. Inset: Plot of normalized increase in absorbance as a function of mole-ratio of calf thymus DNA to [Zn(Cur)]. (C) A modified Scatchard plot for interaction of [Zn(Cur)] with calf thymus DNA; (D) a plot showing $1/\text{fraction of total compound bound}$ vs $1/\text{concentration of calf thymus DNA}$ taken ; [Zn(Cur)] = 41.2 μM , [NaCl] = 150 mM, pH = 7.4 (30 mM phosphate buffer), Temp. = 298K.

The titration data was also fitted to a modified Scatchard equation (Eq. 5, Fig. 10).⁴⁷ K^* and n ($= n_b^{-1}$) were obtained. Values obtained from Eq. 13 were close to that obtained from other methods of analyses (Eq. 9-12, Figs. 9 & 10) justifying techniques that calculate them.

Table 3: Binding parameters for interaction of [Zn(Cur)] with calf thymus DNA at pH = 7.4.

Titration of this complex with DNA is important for a number of reasons. First, since

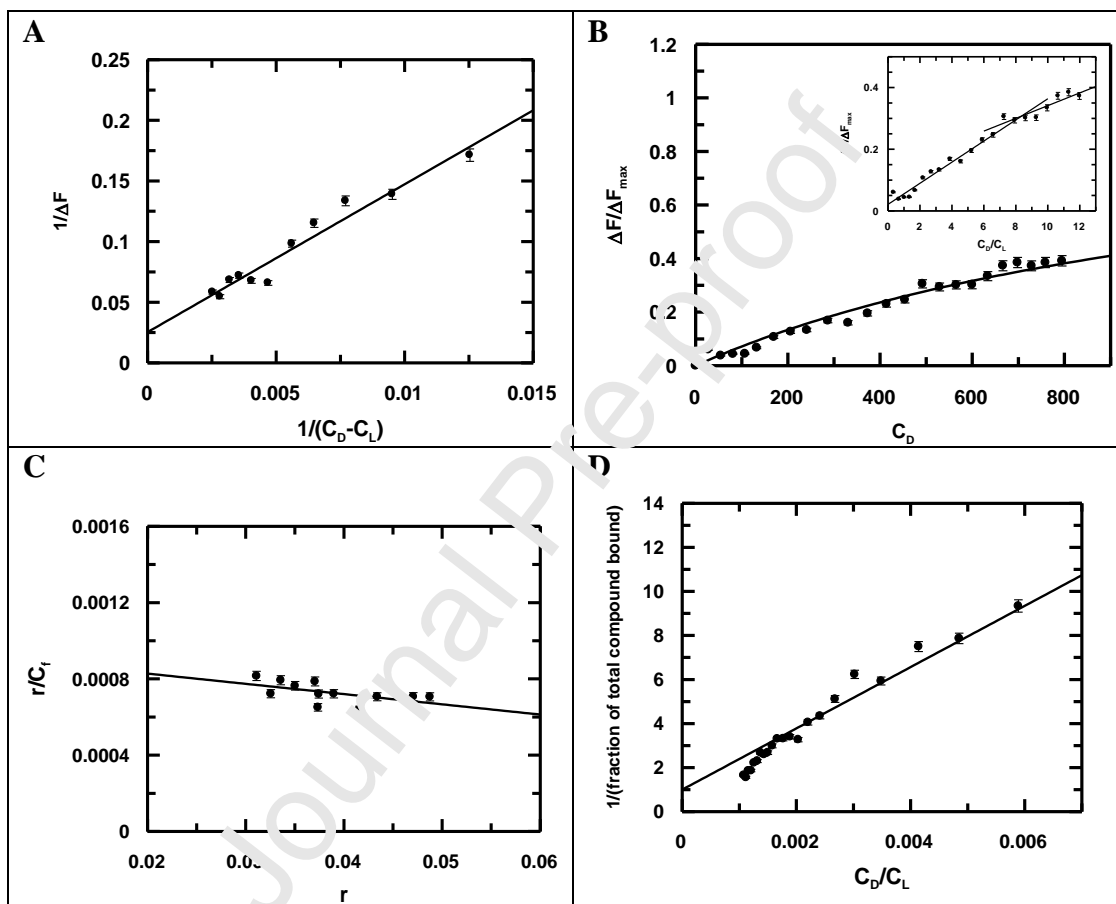
DNA binding methods	No. of Expt.	Apparent binding constant K_{app} (M^{-1})			Site size from mole-ratio plot	Overall binding Constant K^* (M^{-1}) $K^* = K_{app} \times n_b$			Overall binding Constant from Scatchard $\times 10^{-4}$	Site size from Scatchard plot
		Double reciprocal plot $\times 10^{-3}$	Non-linear plot $\times 10^{-3}$	Double reciprocal plot, y-intercept =1 $\times 10^{-3}$		Double reciprocal plot $\times 10^{-4}$	Non-linear plot $\times 10^{-4}$	Double reciprocal plot, y-intercept =1 $\times 10^{-4}$		
	1	2.54	2.51	2.41	10.0	2.54	2.51	2.41	1.86	6.0
Absorbance	2	1.91	1.99	1.89	11.0	2.10	2.19	2.08	2.04	8.0
Fluorescence	1	2.08	1.77	1.42	5.0	1.04	0.90	0.71	1.49	6.0
	2	0.96	0.92	0.72	8.0	0.58	0.55	0.57	0.70	7.0

titration of HCur with DNA has not been possible owing to reasons mentioned earlier, the monomeric complex of Zn^{II} with HCur, where HCur shows no degradation, makes it a model study that in a way represents binding of HCur to DNA.

However, while considering the data, one has to remember that for [Zn(Cur)] there would be an influence of Zn^{II} to binding.^{20, 42-45} Therefore, being able to maintain HCur as a single unit in solution, and that there would be no extra influence due to the coordination compound owing to lack of redox behavior on the part of Zn^{II} , the binding constant value of the coordination compound could well represent HCur.²⁰ Hence, with HCur connected to a metal centre, one can now have an idea of its binding to DNA, that was not possible earlier, Nature, Secondly, from an estimate of binding constant values obtained for [Zn(Cur)] it might become possible to explain some of the mechanisms involved during an interaction of



HCur with DNA (considering HCur as one unit in this coordination compound) and its consequences thereof, during biological interactions, where besides various fragmented forms generated in solution, a substantial portion does remain as one unit.^{12,13,18-20} Hence, together (that is fragmented products of HCur and “HCur as one unit”) it might become



possible to explain a lot of the beneficial activities of HCur.^{12,13,18-20}

Fig : 11 (A) Double reciprocal plot for the interaction of [Zn(Cur)] with calf-thymus DNA to evaluate apparent binding constant (K_{app}), (B) Binding isotherm for [Zn(Cur)] interacting with calf thymus DNA when $\Delta F/\Delta F_{\max}$ was plotted against concentration of DNA; the dark line indicates fitted data obeying Eq. 12. Inset: Plot of normalized increase in absorbance as a function of mole-ratio of calf thymus DNA to [Zn(Cur)]. (C) A modified Scatchard plot for interaction of [Zn(Cur)] with calf thymus DNA; (D) A plot showing $1/\text{fraction of total compound bound}$ vs $1/\text{conc. of calf thymus}$

DNA; [Zn(Cur)] = 82.4 μ M, [NaCl] = 150 mM, pH = 7.4 (30 mM phosphate buffer),
Temp. = 298K.

3.3.2 Computational DNA binding studies

3.3.2.1 Molecular docking studies

Binding modes of [Zn(Cur)] and HCur with desired regions of DNA were established using *in silico* molecular docking. This is a compelling framework for comprehending interactions between compounds and DNA in any rational drug design and for understanding structural characteristics of ligand-receptor complexes, binding energy and affinity of a ligand with its receptors that supports experimental findings. Both molecules were successfully docked with PDB ID: 1BNA having the sequence d(CGCGAATTTCGCG)₂ to undergo extensive molecular mechanics for estimating binding energy and binding affinity of [Zn(Cur)] and HCur with the chosen DNA (PDB ID: 1BNA) (Fig.12 and 13 respectively). Rigid molecular docking was used to determine binding pattern. To forecast optimum molecule-DNA fit and analyze the most energetically advantageous docked position, the molecule was made flexible to achieve several conformations. Autodockvina (version 1.2.3) and Autodock 4.2.6 predicted docking scores of -8.29 Kcal/mole and -7.61 Kcal/mole respectively for HCur with an inhibitory concentration of 2.41 μ M. As shown by 2D and 3D interaction diagrams (Fig. 14 and 15), the nucleotide Gua-10 chain A of DNA formed hydrogen bonds (H-bonds) with HCur's enolic oxygen and hydrogen, measuring 2.06 Å and 1.89 Å respectively. Table S5, SI includes a list of additional interaction modes. It is evident from Fig. 14 (a) that HCur interacts with the chosen DNA.



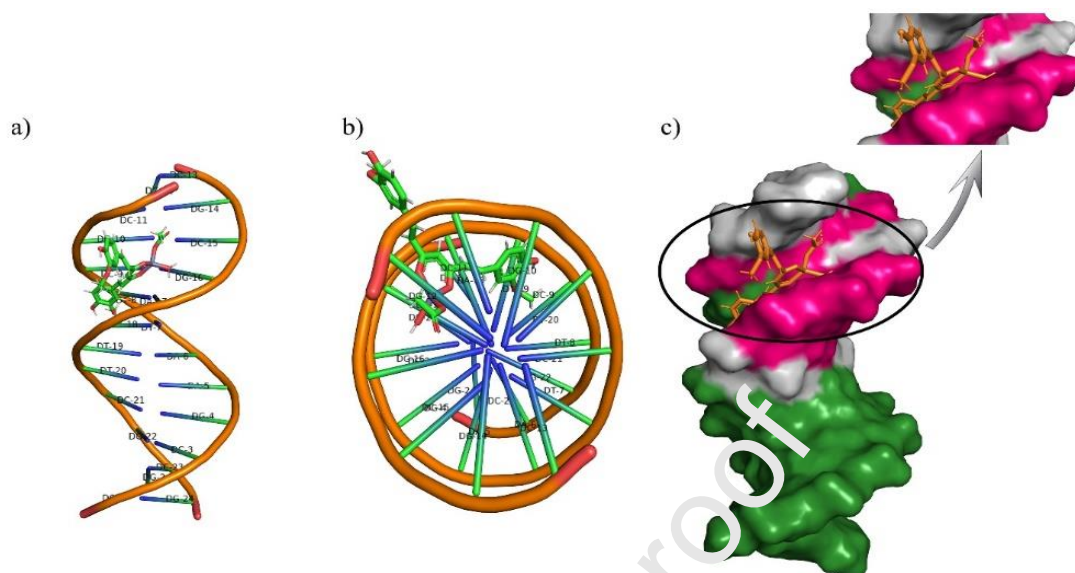


Fig 12: Docked position of [Zn(Cur)] in enol form with DNA (PDB ID :1BNA) (a) side view (b) top view (c) surface view

Docking scores of -8.56 Kcal/mole and -8.36 Kcal/mole respectively were obtained for [Zn(Cur)] anticipated by Autodock vina v1.2.3 and Autodock v4.2.6 with inhibitory concentration $0.7298 \mu\text{M}$. We realized that interacting nucleotides Gua-14(B) (2.43\AA , 2.49\AA), Gua-10(A) (1.88\AA), Gua-16(E) (1.84\AA), Ade-17(B) (2.01\AA) and Ade-18(B) (1.68\AA) form H-bonds. This was obtained from the 2D and 3D interaction diagrams (Fig. 15). Therefore, from binding energy and affinity values (S4, SI) it could be concluded that [Zn(Cur)] interacts with the chosen DNA via intercalation and has greater binding energy than HCur [Fig.12 (b) and Fig.13 (b)]. In Fig. 12 (c) and Fig. 13 (c) magenta indicates all types of polar interactions, green indicates the normal state of the nucleic acid base while white indicates all other weakly interacting regions.

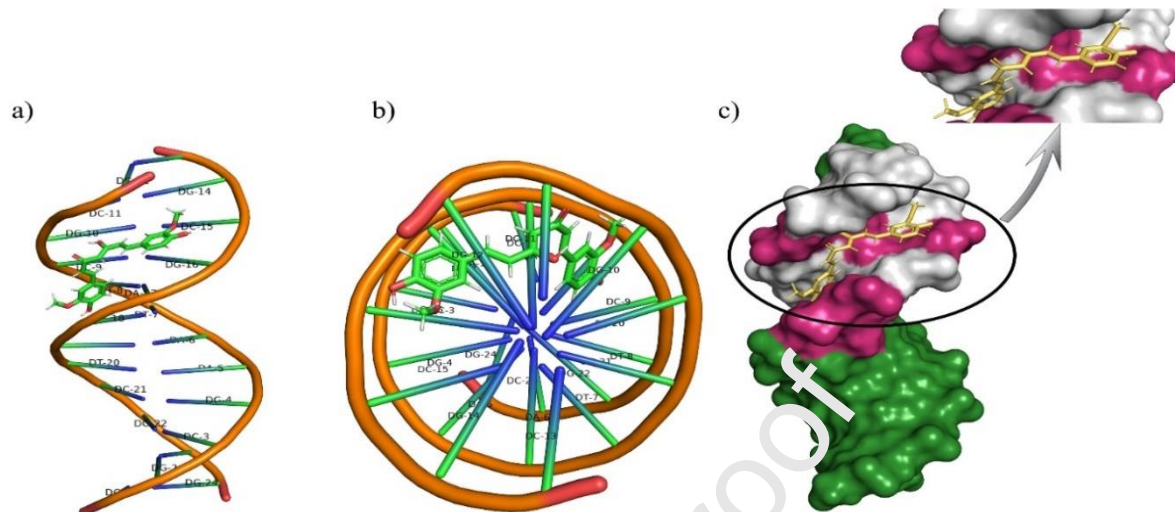


Fig 13: Docked position of HCur with DNA (PDB ID : 1BNA) (a) side view (b) top view (c) surface view

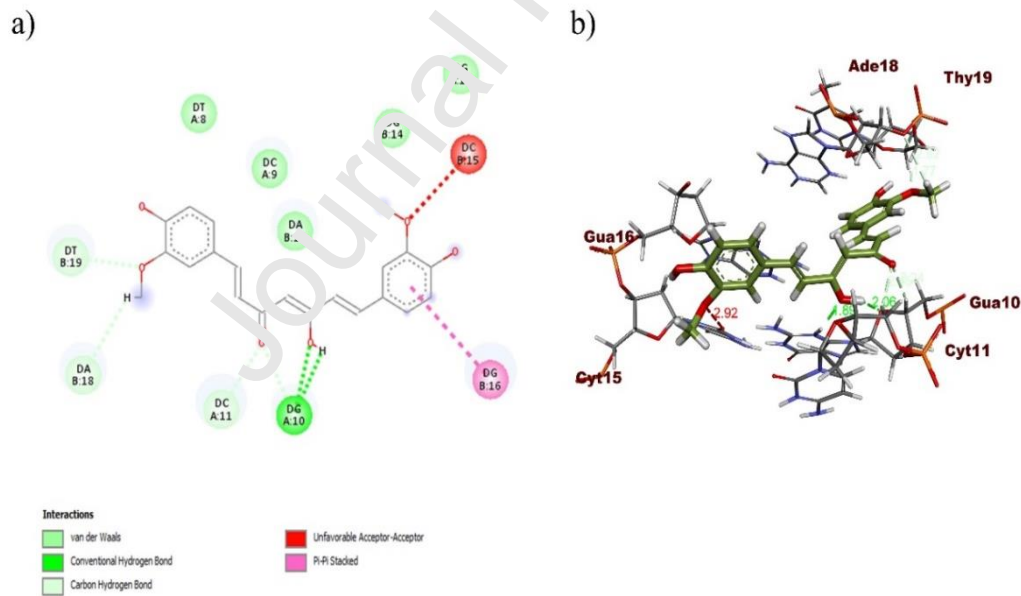


Fig 14: Docked position of HCur with DNA (PDB ID : 1BNA) (a) 2D representation of interactions (b) 3D representation of interactions

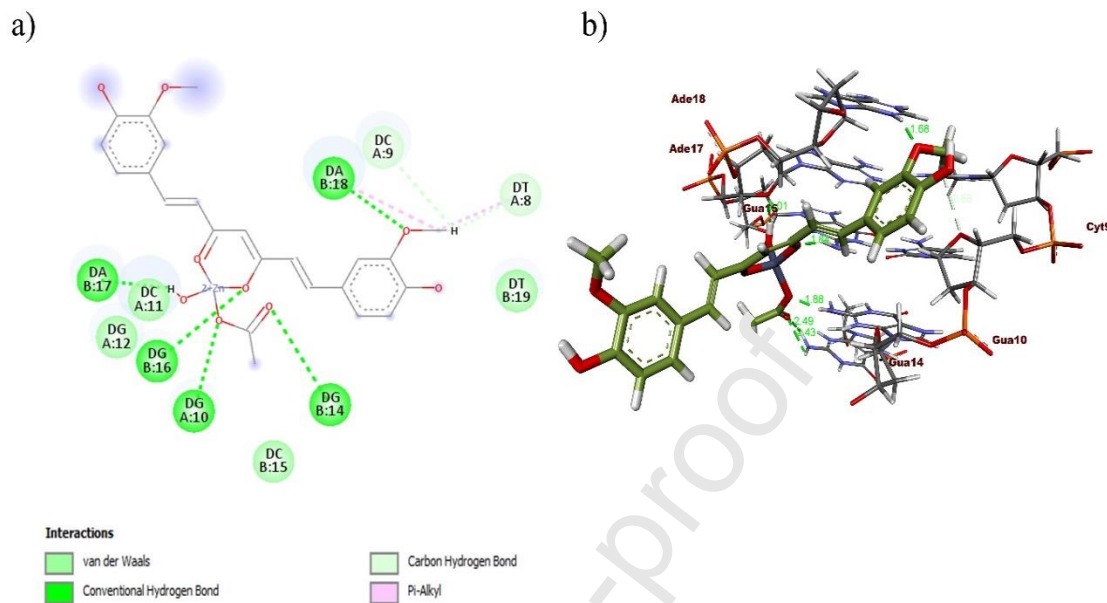


Fig 15: Docked position of [Zn(Cur)] with DNA (PDB ID : 1BNA) (a) 2D representation of interactions (b) 3D representation of interactions

3.3.2.2 Molecular Dynamics

An understanding of the stability of apo-DNA, DNA-HCur and DNA-[Zn(Cur)] guided by root mean square deviation (RMSD) of DNA during the 100 ns simulation provides stability to DNA in an otherwise identical solvent, charge, electrolyte environment. A decrease in RMSD value of DNA is an indication of the extent to which the same DNA is stable in a similar environment. Comparing RMSD trends for simulations followed over 100 ns, both HCur and [Zn(Cur)] docked DNA show stable conformations. Although initially the RMSD values are similar for DNA-[Zn(Cur)], DNA-HCur and DNA itself but as time progressed, tendencies of interactions become different and the one due to DNA-[Zn(Cur)] and DNA-HCur move significantly lower than the red line that denotes RMSD values for DNA itself. This could indicate the Zn compound in its interaction with DNA is very steady on aspects concerning stability; on the other hand,

HCur takes time to adjust, manifested by its observed fluctuations. However, once it has suitably bound itself it also remains steady, so as to match the trend-line for DNA-[Zn(Cur)]. The average RMSD of apo-DNA is 10.67 Å, while for DNA attached to HCur and [Zn(Cur)] they are 9.39 Å and 9.29 Å (Figure 16A) respectively. Unbound DNA with a higher RMSD has therefore undergone more conformational change in its two chains, A and B. The fact that RMSD reduces when HCur and [Zn(Cur)] are bound to DNA indicates they form stable adducts with DNA that can withstand further conformational changes within DNA. A lower RMSD of [Zn(Cur)] with DNA suggests higher stability of the complex than HCur-DNA.

In our case, the Root Mean Square Fluctuation (RMSF) would be a measure of the motion of a nucleobase around its mean position along the trajectory of MD simulation. It should indicate flexibility of some portions of the chosen DNA (1PNA). RMSF of the bound form of HCur with 1BNA is similar to that of 1BNA itself, particularly in the region of residue index 10-15, while that of [Zn(Cur)] bound 1BNA shows significantly lower fluctuation in the same region (Fig. 16 B). The RMSF plot of [Zn(Cur)] exhibit a significantly lower nature than that for HCur, clearly indicating positional fluctuations of nucleobases were more in the other two states as compared to the [Zn(Cur)] derived bound state.

In molecular dynamics simulation, radius of gyration (Rg) measures how compact the receptor is upon binding to a ligand. Lower Rg values imply the ligand is more compact inside the receptor cavity, thus stabilizing the adduct. In this investigation, DNA linked to [Zn(Cur)] initially showed somewhat increased displacements between 17 to 20 ns, but thereafter, it became stable (Figure 16 C). Contrarily, HCur bound to DNA exhibits variability between 20 to 80 ns that denote less efficient binding. Significantly stable gyration (Rg) of [Zn(Cur)] with DNA suggests that the DNA is oriented in a highly compact manner when attached to [Zn(Cur)].



SASA was determined using the entire atom's 100 ns molecular dynamics journey and plotted against time (Figure 16 D). An understanding of the ligand's location within the binding pocket could be had through an analysis of SASA parameters. One might think of ligand binding to a receptor cavity as that of a solvent replacement effect. A lower SASA value compared to apo-DNA suggest that the ligand is present in the binding pocket.

When HCur was bound to DNA, the average SASA value was 558.613 \AA^2 , while when [Zn(Cur)] was attached, the average SASA value was 455.654 \AA^2 . These values are significantly lower than when compounds were not bound to DNA (896.270 \AA^2). Again, it may be noted that decrease in average SASA value was significantly lower in case of [Zn(Cur)] than in case of HCur. Based on our findings mentioned above, it may be concluded [Zn(Cur)] has a higher affinity for DNA and that it intercalates after 100 ps simulation (Fig. 16D).

Number of hydrogen bonds between DNA and HCur or [Zn(Cur)] shows adducts (i. e. complexes) have significant interaction and that they are stable. As simulation continued for 100 ns, there were considerable number of hydrogen bonds between DNA and HCur or [Zn(Cur)] (Figure 16E). In Figure 16E, an average of three hydrogen bonds were seen forming between DNA and [Zn(Cur)] over the course of 100 ns simulation detecting molecules achieving stable associated species. In contrast, only one hydrogen bond was formed between DNA and HCur in the same time scale of simulation.

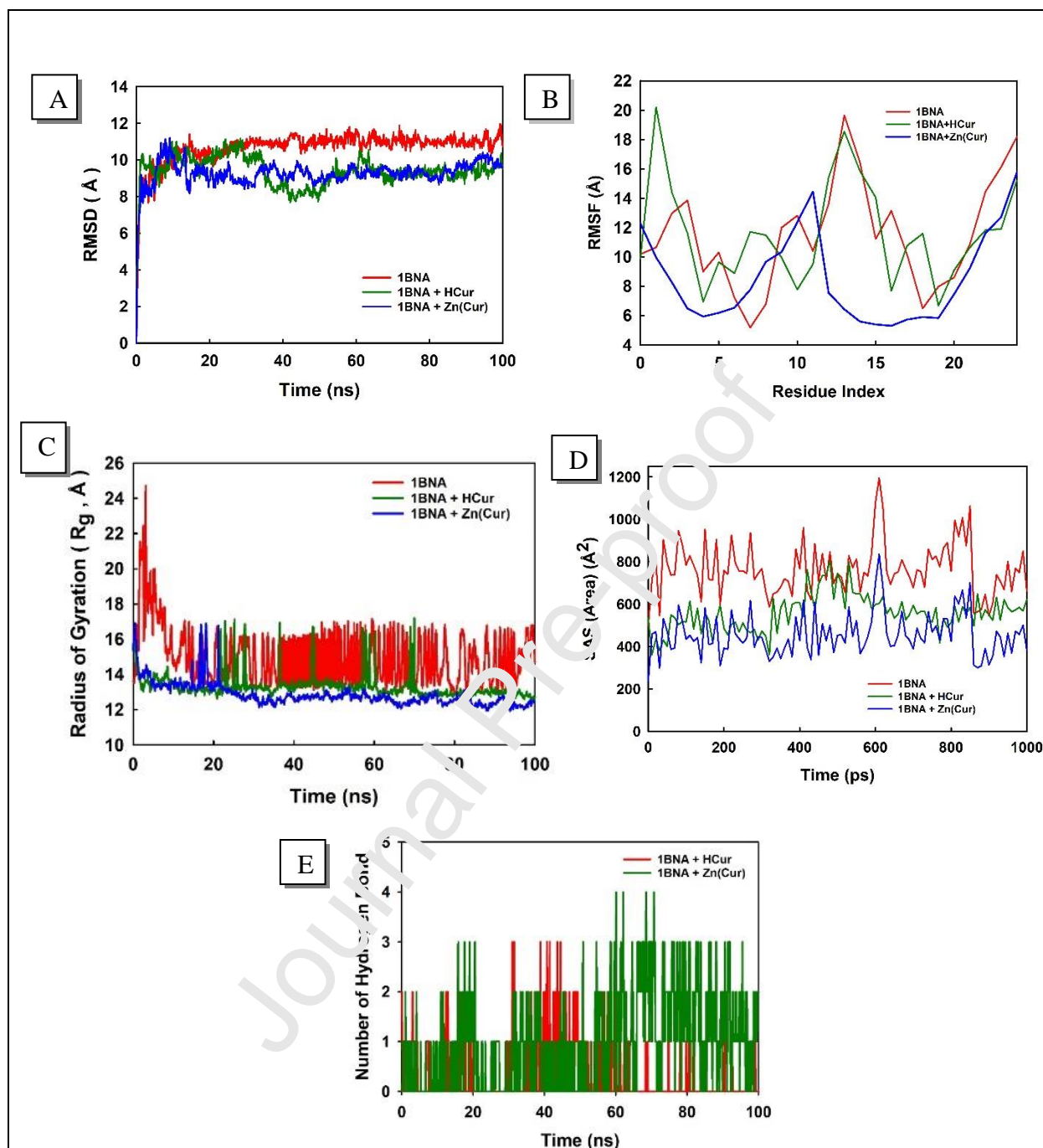


Fig 16: (A) RMSD plot of free DNA (PDB ID : 1BNA), DNA with HCur and DNA with [Zn(Cur)], (B) RMSF plot of free DNA (PDB ID : 1BNA), DNA with HCur and DNA with [Zn(Cur)], (C) Radius of gyration plot of free DNA (PDB ID : 1BNA), DNA with HCur and DNA with [Zn(Cur)], (D) SASA and (E) Hydrogen bonding plots of HCur and [Zn(Cur)] formed with DNA during simulation.

This suggests associated structures formed by [Zn(Cur)] are more stable than that formed by HCur with the same DNA background (PDB ID-1BNA). The interaction of [Zn(Cur)] with 1BNA at the first frame (0 ns), an intermediate frame (50 ns) and last frame (100 ns) is provided in Fig. 17. From the three figures, it is clearly evident that [Zn(Cur)] binding is one of intercalation as the compound tries to position itself between the strands of DNA. This signifies [Zn(Cur)] is well docked at a site of 1BNA that has been further confirmed by MM-GBSA calculations (Table 4).

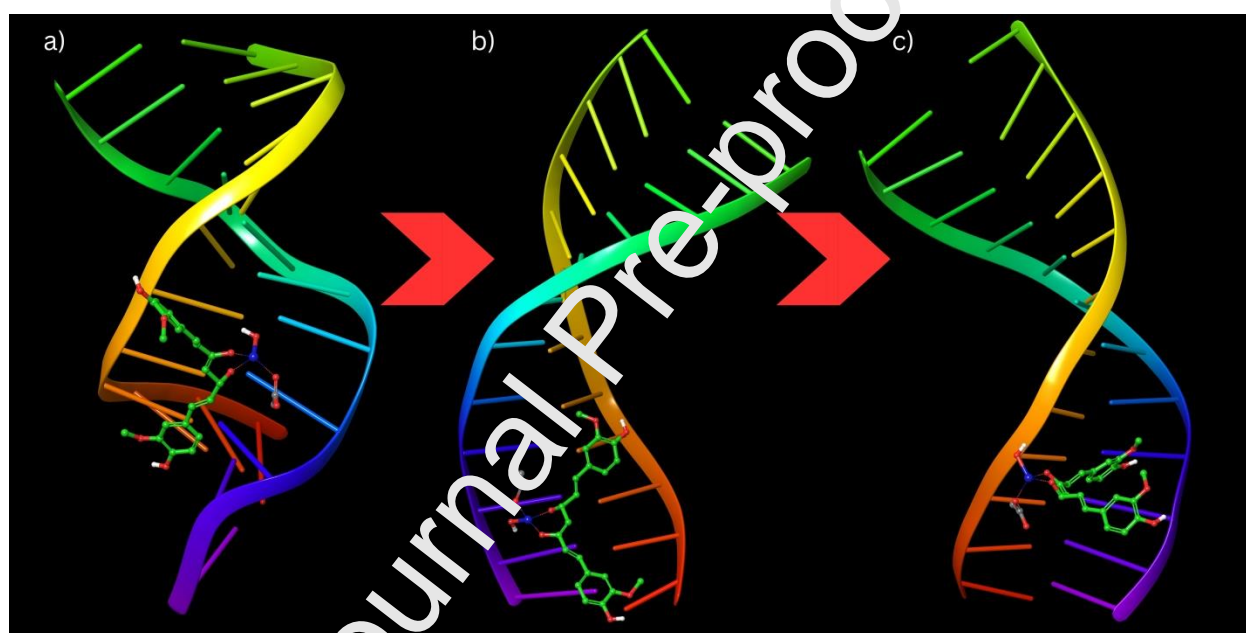


Fig 17: Structural superimposition of (a) first frame (0 ns); (b) an intermediate frame (50 ns) and (c) last frame (100ns) of [Zn(Cur)] bound with 1BNA after simulation

3.3.2.3 Molecular Mechanics Generalized Born Surface Area (MM-GBSA) calculations

Utilizing the molecular dynamic simulation trajectory, binding free energy along with other contributing energies in the form of MM-GBSA were determined for DNA-HCur and DNA-[Zn(Cur)] complex systems. Results in Table 4 suggest that maximum contribution to $\Delta G_{\text{binding}}$ for stability of the simulated compounds were due to $\Delta G_{\text{bind-coulomb}}$, $\Delta G_{\text{bind-van der waals}}$ and

$\Delta G_{\text{bind-lipophilic}}$ while $\Delta G_{\text{bind-covalent}}$ and $\Delta G_{\text{bind-solvation}}$ contribute to instability. $\Delta G_{\text{binding}}$ for DNA-[Zn(Cur)] complex was comparatively more negative in terms of free energy than DNA-HCur. These results support the potential of [Zn(Cur)] over HCur in binding DNA and showed efficiency of binding to the selected DNA and an ability to form stable DNA-ligand complexes.

Table 4. Binding free energy components for the DNA-HCur and DNA-[Zn(Cur)] complexes calculated by MM-GBSA.

Compound code	MM-GBSA (kcal/mol)					
	ΔG_{bind}	$\Delta G_{\text{bindLipo}}$	$\Delta G_{\text{bindvdW}}$	$\Delta G_{\text{bindCoulomb}}$	$\Delta G_{\text{bindSolvGB}}$	$\Delta G_{\text{bindCovalent}}$
DNA-HCur	-46.50± 6.35	-17.13± 1.23	-47.29 ± 2.17	-0.2151± 5.54	35.97± 2.78	2.76± 1.90
DNA-[Zn(Cur)]	-50.89± 2.28	-21.53± 3.54	-51.28± 1.25	0.5154± 4.20	46.58± 3.24	1.75± 2.50

(G_{bind}) total free energy of binding; (G_{bindLipo}) lipophilic energy; (G_{bindvdW}) van der Waals interaction energy; ($G_{\text{bindCoulomb}}$) prime coulomb energy; ($G_{\text{bindSolvGB}}$) solvation energy generalized born; ($G_{\text{bindCovalent}}$) covalent binding energy

4. Conclusion:

The present study suggests MD simulation and binding free energy calculations are in good agreement with docking studies and that they exhibit properties of higher binding and probable inhibition of DNA in its functional role in the bio-system. Theoretical studies corroborate an experimental DNA binding study that was done using calf thymus DNA. Hence, such compounds may be considered as potential drug candidates against DNA since they target the DNA moiety and inhibit activities like replication and transcription that play crucial roles for stopping the growth of cells.

5. Acknowledgments:



SD wish to thank “RUSA 2.0” program of Government of India, operating at Jadavpur University through which he received a grant "Research Support to Faculty Members" in the thrust area "Research in Sustainable Development" (Sanction Ref. no. R-11/438/19 dated 30.05.2019). SS wishes to gratefully acknowledge Gdańsk University of Technology for Nobelium (No. 16/2021/IDUB/I.1) grant under “The Excellence Initiative – Research University” (IDUB) program. TS gratefully acknowledge Dr. Soumen Singha of the Department of Physics, Jadavpur University for his help and cooperation with regard to DFT calculations. He wishes to thank the “Governing Body” of Sri Aurobindo Institute of Education, Salt Lake, Kolkata for their support in his research endeavours.

References:

1. Aggarwal, B. B., Sundaram, C., Malani, N. and Ichikawa, H. Curcumin: The Indian solid gold. In: *The molecular targets and therapeutic uses of curcumin in health and disease* (pp. 1-75). Springer, Boston, MA, (2007).
2. Jurenka, J. S. Anti-inflammatory properties of curcumin, a major constituent of *Curcuma longa*: a review of preclinical and clinical research. *Alternative Medicine Review*, 2009, **14**, 141-153.
3. Ak, T. and Gülçin, İ. Antioxidant and radical scavenging properties of curcumin. *Chem-biol. Inter.*, 2008, **174**, 27-37.
4. Wilken, R., Veena, M. S., Wang, M. B. and Srivatsan, E. S. Curcumin: A review of anti-cancer properties and therapeutic activity in head and neck squamous cell carcinoma. *Mol. Cancer*, 2011, **10**:12. doi: 10.1186/1476-4598-10-12.



5. Wanninger, S., Lorenz, V., Subhan, A. and Edelman, F. T. Metal complexes of curcumin–synthetic strategies, structures and medicinal applications. *Chem. Soc. Rev.* 2015, **44**, 4986-5002.
6. Teow, S. Y., Liew, K., Ali, S. A., Khoo, A. S. B. and Peh, S. C. Antibacterial action of curcumin against *Staphylococcus aureus*: a brief review. *Jour. Trop. Med.*, 2016, 2016 Article ID 2853045, 10 pages; <https://doi.org/10.1155/2016/2853045>.
7. Goel, A., Kunnumakkara, A. B. and Aggarwal, B. B. Curcumin as “Curcumin”: from kitchen to clinic. *Biochem. Pharmacol.*, 2008, **75**, 787-802.
8. Neelofar, K., Shreaz, S., Rimple, B., Muralidhar, S., Nikhat, M., Khan, L. A. Curcumin as a promising anticandidal of clinical interest. *Curr. Jour. Microbiol.* 2011, **57**, 204-210.
9. Tyagi, P., Singh, M., Kumari, H., Kumari, A., Mukhopadhyay, K. Bactericidal activity of Curcumin I is associated with damaging of bacterial membrane. 2015, *PloS one* 10, e0121313.
10. Sharma, R. A., Steward, W. P., Gescher, A. J. Pharmacokinetics and pharmacodynamics of Curcumin. *Adv. Exp. Med. Biol.* 2007, **595**, 453-470.
11. Banerjee, R. Inhibitory effect of Curcumin-Cu(II) and Curcumin-Zn(II) complexes on amyloid-beta peptide fibrillation, *Bioinorg. Chem. Appl.* **2014**, 325873 (2014).
12. Saha, T., Kumar, P., Sepay, N., Ganguly, D., Tiwari, K., Mukhopadhyay, K., Das, S. Multitargeting antibacterial activity of a synthesized Mn²⁺ complex of Curcumin on gram-positive and gram-negative bacterial strains. *ACS Omega*, 2020, **5**, 27, 16342–16357.
13. Banerjee, S., Prasad, P., Hussain, A., Khan, I., Kondaiah, P., Chakravarty, A. R. Remarkable photocytotoxicity of curcumin in HeLa cells in visible and arresting its



- degradation on oxovanadium (IV) complex formation. *Chem. Comm.* 2012, **48**, 7702-7704.
14. Priyadarsini K. I. The chemistry of Curcumin: From extraction to therapeutic agent. *Molecules*, 2014, **19**, 20091-20112.
15. Cas M. D. and Ghidoni, R. Dietary Curcumin: Correlation between bioavailability and health potential, *Nutrients*. 2019, 11(9), 2147; <https://doi.org/10.3390/nu11092147>.
16. de Souza Ferreira S. B. and Bruschi M. L. Improving the bioavailability of curcumin: is micro/nanoencapsulation the key?, *Ther Deliv.* 2019, **10**, 23-86; doi: 10.4155/tde-2018-0075.
17. Anand, P., Kunnumakkara, A. B., Newman, P. A., Aggarwal, B. B. Bioavailability of Curcumin: Problems and promises, *Molecular Nutrition* 2007, **4**, 807–818.
18. Kumar, P.; Saha, T.; Behera, S.; Gupta, S.; Das, S.; Mukhopadhyay, K. Enhanced efficacy of a Cu²⁺ complex of curcumin against gram positive and gram-negative bacteria: Attributes of complex formation, *Jour. Inorg. Biochem.*, 2021, **222**,111494.
19. Wang, Y.-J. Pan, M.-H., Cheng, A.-Li, Lin, L.-I., Ho, Y.-S., Chang-Yao Hsieh, Jen-Kun Lin. Stability of curcumin in buffer solutions and characterization of its degradation products. *J. Pharma. Biomed. Anal.* 1997, **15**, 1867-1876.
20. Saha, T., Singha, S., Kumar, S., Das, S. Spectroscopy driven DFT computation for a structure of the monomeric Cu²⁺-Curcumin complex and thermodynamics driven evaluation of its binding to DNA: Pseudo-binding of Curcumin to DNA. *Jour. Mol. Struc.*, 2020, **1221**, 128732.
21. Enhancement of anti-leukemic potential of 2-hydroxyphenyl-azo-2'-naphthol (HPAN) on MOLT-4 cells through conjugation with Cu(II), *RSC Adv.*, 2014, **4**,18419-18430.



22. Moghadam, K. S., Toroghi, E. S., Vatanparast, K. M., Jouyaeian, P., Mokaberi, P., Yazdyani, H., Tehranizadeh, A. Z., Saberi, R. M., Chamani, J. Novel perspective into the interaction behavior study of the cyanidin with human serum albumin-holo transferrin complex: Spectroscopic, calorimetric and molecular modeling approaches, *Journal of Molecular Liquids*, 2022, **356**, 119042.
23. Darban, A. R., Shareghi, B., Asoodeh, A., Chamani, J., Multi-spectroscopic and molecular modeling studies of interaction between two different angiotensin I converting enzyme inhibitory peptides from gluten hydrolysate and human serum albumin, *Jour. Biomol.Struc. Dyns.*, 2017, **35(16)**, 3648-3662.
24. Dhanaraj, C J.; Hassan, I U.; Johnson, J.; Joseph, J.; Joseyphus, R S. Synthesis, spectral characterization, DNA interaction, anticancer and molecular docking studies on some transition metal complexes with bidentate ligand, *Jour. Photochem. Photobiol. B: Biology*, 2016, **162**, 115-124.
25. Marjani N, Dareini M, Asadzade-Lotfabad M, Pejhan M, Mokaberi P, Amiri-Tehranizadeh Z, Saberi MR, Chamani J. Evaluation of the binding effect and cytotoxicity assay of 2-Ethyl-5-(4-methylphenyl) pyrimido pyrazole ophthalazine trione on calf thymus DNA: spectroscopic, calorimetric, and molecular dynamics approaches. *Luminescence*, 2022, **37(2)**, 310-322.
26. Feizabadi, Z. N., Tehranizadeh, A. Z., Rad, S. A., Mokaberi, P., Nosrati, N., Hashemzadeh, F., Rahimi, R. H., Saberi, R. M., Chamani, J. Determining the interaction behavior of calf thymus DNA with anastrozole in the presence of histone H1: Spectroscopies and cell viability of MCF-7 cell line investigations, *DNA and Cell Biology* 2021, **40(8)**, 1039-1051.



27. Maheri, H., Hashemzadeh, F., Shakibapour, N., Kamelniya, E., Nikouei, M.B., Mokaberi, P., Chamani, P., Glucokinase activity enhancement by cellulose nanocrystals isolated from jujube seed: A novel perspective for type II diabetes mellitus treatment (In vitro), *Jour. Mol. Struc.*, 2022, **1269**, 133803.
28. Spinello, A., Terenzi, A., Barone G. Metal complex-DNA binding: Insights from molecular dynamics and DFT/MM calculations. *Jour. Inorg. Biochem.* 2013, **124**, 63-69.
29. Masztafiak, J. C. et. al. Direct Determination of metal complexes's interaction with DNA by atomic telemetry and multiscale molecular dynamics. *Jour. Phys. Chem. Lett.*, 2017, **8**, 805-811.
30. Characterization of the structural changes of human serum albumin upon interaction with single-walled and multi-walled carbon nanotubes: spectroscopic and molecular modeling approaches, *Res. Chem. Inter.*, 2019, **45**, 401-423.
31. Chamani J., Moosavi-Movahedi, G. H., Hakimelahi, A. A. Structural changes in β -lactoglobulin by conjugation with three different kinds of carboxymethyl cyclodextrins, *Thermochimica acta*, 2005, **432**, 106-111.
32. Frisch, M. J., Trucks, G. W., Schlegel, H. B., Scuseria, G. E., Robb, M. A., Cheeseman, J. R., Scalmani, G., Barone, V., Petersson, G. A., Nakatsuji, H., Li, X., Caricato, M., Marenich, A. V., Bloino, J., Janesko, B. G., Gomperts, R., Mennucci, B., Hratchian, H. P., Ortiz, J. V., Izmaylov, A. F., Sonnenberg, J. L., Williams-Young, D., Ding, F., Lipparini, F., Egidi, F., Goings, J., Peng, B., Petrone, A., Henderson T., Ranasinghe, D., Zakrzewski, V. G., Gao, J., Rega, N., Zheng, G., Liang, W., Hada, M., Ehara, M., Toyota, K., Fukuda, R., Hasegawa, J., Ishida, M., Nakajima, T., Honda, Y., Kitao, O.,



- Nakai, H., Vreven, T., Throssell, K., Montgomery Jr., J. A., Peralta, J. E., Ogliaro, F., Bearpark, M. J., Heyd, J. J., Brothers, E. N., Kudin, K. N., Staroverov, V. N., Keith, T. A., Kobayashi, R., Normand, J., Raghavachari, K., Rendell, A. P., Burant, J. C., Iyengar, S. S., Tomasi, J., Cossi, M., Millam, J. M., Klene, M., Adamo, C., Cammi, R., Ochterski, J. W., Martin, R. L., Morokuma, K., Farkas, O., Foresman, J. B., Fox, D. J. Gaussian 09, Revision D.01, Gaussian, Inc., Wallingford CT, 2016.
33. (a) Becke, A. D. Density-functional thermochemistry. III. The role of exact exchange, *J. Chem. Phys.* 1993, **98**, 5648e5652; (b) Lee, C. E., Yang, W. T., Parr, R. G. Development of the Colle-Salvetti correlation-energy formula into a functional of the electron density, *Phys. Rev. B* 1988, **37**, 785e789.
34. Chiodo, S., Russo, N., Sicilia, E., LANL 2TZ basis sets recontracted in the framework of density functional theory, *Jour. Chem. Phys.* 2006, **125**, 104107.
35. Cossi, M., Barone, J. V., Time dependent density functional theory for molecules in liquid solutions, *Chem. Phys.* 2001, **115**, 4708e4717.
36. Gross, E. K. U. and Kohn, W. Time-dependent density functional theory in, *Adv. Quant. Chem.* 1990, **21**, 255e291.
37. O'Boyle, N. M., Tenderholt, A. L., Langner, K. M. Cclib: a library for package independent computational chemistry algorithms, *J. Comput. Chem.* 2008, **29**, 839-845.
38. Choudhary, V. K., Bhatt, A. K., Dash, D., Sharma, N. DFT calculations on molecular structures, HOMO-LUMO study, reactivity descriptors and spectral analyses of newly synthesized diorganotin(IV) 2-chloridophenylacetohydroxamate complexes, *Jour. Comp. Chem.* 2019, 1-10.



39. Otero-de-la-Roza, A., Johnson, E.R., and Contreras-García, J. Revealing non-covalent interactions in solids: NCI plots revisited, *Physical Chemistry, Chemical physics*, 2012, 35.
40. Lu, T., Chen, F. Multiwfn: A multifunctional wavefunction analyzer. *Jour. Comput. Chem.*, 2012, **33**, 580-592.
41. Kumar, A., Yeole, S. D., Gadre, S. R., Lopez, R., Rico, J.F., Ramirez, G., Ema, I. Zorrilla, D. DAMQT 2.1.0: A new version of the DAMQT package enabled with the topographical analysis of electron density and electrostatic potential in molecules. *Jour. Comput. Chem.* 2015, **36**, 2350-2359.
42. Deb, T., Choudhury, D., Guin, P. S., Saha, M. B., Chakrabarti, G., Das, S. A complex of Co(II) with 2-hydroxyphenyl-azo-2'-naphthol (HPAN) is far less cytotoxic than the parent compound on A549-lung carcinoma and peripheral blood mononuclear cells: Reasons for reduction in cytotoxicity. *Chem-Biol. Inter.* 2011, **189**, 206-214.
43. Guin, P. S., Mandal, P. C., Das, S. The binding of a hydroxy-9,10-anthraquinone Cu^{II} complex to calf thymus DNA: Electrochemistry and UV/Vis spectroscopy, *ChemPlusChem*, 2012, **7**, 361-369; <https://doi.org/10.1002/cplu.201100046>.
44. Das, P., Jain, C. K., Dey, S. K., Saha, R., Chowdhury, A. D., Roychoudhury, S., Kumar, S., Majumder, H. K., Das, S. Synthesis, crystal structure, DNA interaction and *in vitro* anticancer activity of a Cu(II) complex of purpurin: dual poison for human DNA topoisomerase I and II. *RSC Adv.*, 2014, **4**, 59344-59357.
45. Mandal, B., Singha, S., Dey, S. K., Mazumdar, S., Mondal, T. K., Karmakar, P., Kumar, S., Das, S. Synthesis, crystal structure from PXRD of a Mn^{II}(purp)₂ complex, interaction with DNA at different temperatures and pH and lack of stimulated ROS formation by the complex, *RSC Adv.* 2016, **6**, 51520–51532.



46. Mukherjee-Chatterjee, S., Jain, C. K., Singha, S., Das, P., Roychoudhury, S., Majumder, H. K., Das, S. Activity of Co^{II}-Quinalizarin: A novel analogue of anthracycline-based anticancer agents targets human DNA topoisomerase, whereas quinalizarin itself acts via formation of semiquinone on acute lymphoblastic leukemia MOLT-4 and HCT 116 cells. *ACS Omega*, 2018, **3**, 10255-10266.
47. Scatchard, G. The attractions of proteins for small molecules and ions. *Ann. N. Y. Acad. Sci.*, 1949, **51**, 660–672.
48. Morris, G. M., Huey, R., Lindstrom, W., Sanner, M. F.,蓀erson, R. K., Goodsell, D. S. and Olson, A. J. Auto dock4 and Auto dock tools 4: Automated docking with selective receptor flexibility. *Jour. Comput. Chem.*, 2009, **16**, 2785-2791.
49. Eberhardt, J., Santos-Martins, D., Tillack, A F., Frcili, S. AutoDock Vina 1.2.0: New docking methods, expanded force field, and python bindings. *Jour. Chem. Inf. Model.* **2021**, **61**, 8, 3891–3898.
50. Trott, O. and Olson, A. J. Auto Dock Vina: Improving the speed and accuracy of docking with a new scoring function, efficient optimization, and multithreading. *Jour. Comp. Chem.*, **2010**, **31**, 455-461.
51. Huey, R., Morris, G. M., Olson, A. J., Goodsell, D. S. A semiempirical free energy force field with charge-based desolvation. *Jour. Comp. Chem.*, 2007, **28**, 1145-1152.
52. Drew, H. R., Wing, R. M., Takano, T., Broka, C., Tanaka, S., Itakura, K. Dickerson, R. E., Structure of a B-DNA dodecamer: Conformation and dynamics, *Proc. Nat. Acad. Sci. USA*, **1981**, **78**, 2179-2183.



53. Ghosh, A., Mukerjee, N., Sharma, B., Pant, A., Mohanta, K. Y., Jawarkar, R. D. Target specific inhibition of protein tyrosine kinase in conjunction with cancer and SARS-COV-2 by olive nutraceuticals, *Fronts. Pharmacol.*, **2022**, 12.
54. Patra, D., Paul, S., Sepay, N., Kundu, R., Ghosh, T. Structure-activity relationship on DNA binding and anticancer activities of a family of mixed ligand oxidovanadium (V) hydrazone complexes, *Jour. Biomol. Struct. Dyn.* 2017, **36**, 4143-4155.
55. Shaw, D E, Research Desmond, www.deshawresearch.com; https://www.deshawresearch.com/downloads/download_descmond.cgi/
56. Shivakumar, D., Williams, J., Wu, Y., Damm, W., Shelley, J., Sherman, W. Prediction of absolute solvation free energies using Molecular Dynamics free energy perturbation and the OPLS force field, *Journal of Chemical theory and computation*, **2010**, 65, 1509-1519.
57. Jorgensen, W.L., Chandrasekhar, J., Madura, D. Comparison of simple potential functions for simulating liquid water, *J.Chem.Phys*, **1983**, 79, 926.
58. Martyna, G. J., Klein, M.I. Nose Hoover chains: The canonical ensemble via continuous dynamics. *Jour. Chem. Phys*, **1992**, 97, 2635-2643.
59. Martyna, G. J., Tobias, D. J., Klein, M.L. Constant pressure molecular dynamics algorithms. *Jour. Chem. Phys*, **1994**, 101, 4177-4189.
60. Toukmaji, A.Y., Board, J.A. Ewald summation techniques in perspective: a survey, *Computer physics communications*, **1996**, 95, 2-3, 73-92.
61. Zaki, M. E. A.; Al-Hussain, S. A.; Masand, V. H.; Akasapu, S.; Bajaj, S. O.; El-Sayed, N. N. E.; Ghosh, A., Lewaa, I. Identification of anti-SARS-CoV-2 compounds from food using QSAR-based virtual screening, molecular docking, and molecular dynamics simulation analysis. *Pharmaceuticals*, 2021, **14**, 357; doi: 10.3390/ph14040357.



62. Genheden S, Ryde U. The MM/PBSA and MM/GBSA methods to estimate ligand-binding affinities. *Exp. Opin. Drug Discovery* 2015, 5, 449-61.
63. Choudhary, M. I., Shaikh, M., Tul-Wahab, A., & Ur-Rahman, A., *In silico* identification of potential inhibitors of key SARS-CoV-2 3CL hydrolase (Mpro) via molecular docking, MMGBSA predictive binding energy calculations, and molecular dynamics simulation. *Plos one*, 2020, **15(7)**, e0235030.
64. Grabner, S., Modec, B. Zn(II) Curcuminato complexes with 2, 2'-bipyridine and carboxylates molecules, *Molecules* 2019, 24, 2540; <https://doi.org/10.3390/molecules24142540>.
65. Chattaraj, P. K., Giri, S., Electrophilicity index within a conceptual DFT framework, *Annu. Reports Sect. 'C' Phys. Chem.*, 2009, **105**, 13-39.
66. Chattaraj P. K., Sarkar, U., Roy D. R., Electrophilicity index, *Chem. Rev.* 2006, **106**, 2065–2091.
67. Ghosh, M., Sepay, N., Rizzol C., Ghosh, C. K., Banerjee, A., Saha, S. Mononuclear copper (II) schiff base complex: Synthesis, structure, electrical analysis and protein binding study, *New J. Chem*, **2021**, 45, 2995-3006.



Author Statement

The following is an author statement outlining all authors' individual contributions using relevant CRediT roles for manuscript having Manuscript Number: IJBIOMAC-D-23-02305

Tanmoy Saha: Conceived and designed the experiments; performed them; analyzed and interpreted the data.

Subrahmanyam Sappati: Conceived and designed the experiments; performed them; analyzed and interpreted the data.

Saurabh Das: Conceived and designed experiments; analyzed and interpreted the data; wrote the paper.

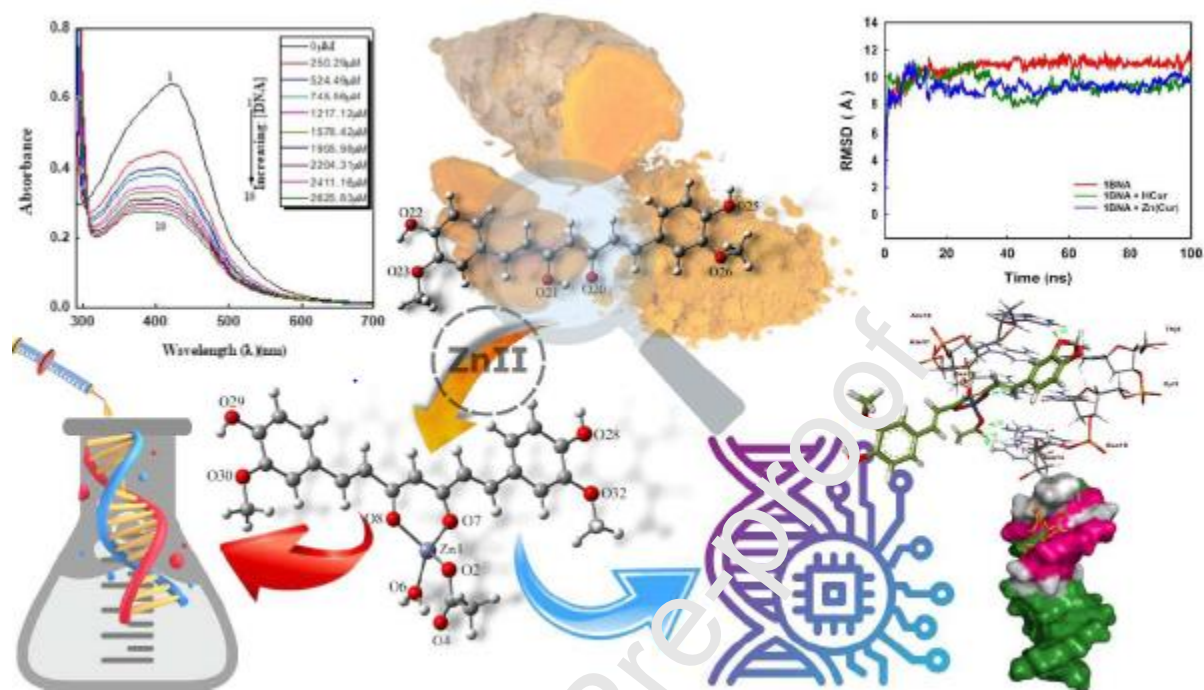
Declaration of interests

The authors declare that they have no known competing financial interests or personal relationships that could have appeared to influence the work reported in this paper.

The authors declare the following financial interests/personal relationships which may be considered as potential competing interests:

Journal Pre-proof

Graphical abstract



Highlights

- 1) Unlike Curcumin, Zn^{II} complex, $[Zn(Cur)]$ was found to be very stable at physiological pH,
- 2) $[Zn(Cur)]$ is monomeric, tetrahedral, having one Curcumin, an acetate and one water molecule.
- 3) Structure was obtained with the help of DFT calculations.
- 4) Experimental DNA binding leads to evaluation of binding constants for the complex.
- 5) Molecular docking was carried out for $[Zn(Cur)]$ with DNA to visualize 2D and 3D interactions.
- 6) Molecular dynamics simulation revealed detailed understanding of binding pattern.
- 7) Binding of $[Zn(Cur)]$ with DNA represents binding of undissociated Curcumin to DNA.
- 8) Theoretical studies on DNA identify Curcumin's affinity for cells; experimentally unrealized.

